The Astrophysical Journal, 998:147 (22pp), 2026 February 10 https://doi.org/10.3847/1538-4357/ae336c

On the Deepest Search for Galactic Center Pulsars and an Examination of an Intriguing Millisecond Pulsar Candidate

Karen I. Perez[1,2], Vishal Gajjar[2,3], Slavko Bogdanov[4], Jules P. Halpern[1,4], Paul B. Demorest[5], Steve Croft[2,3,6], Matt Lebofsky[3], David H. E. MacMahon[3], and Andrew P. V. Siemion[2,3,6,7,8]
[1] Department of Astronomy, Columbia University, 550 West 120th Street, New York, NY 10027, USA; karen.i.perez@columbia.edu
[2] SETI Institute, 339 Bernardo Avenue, Suite 200, Mountain View, CA 94043, USA
[3] Breakthrough Listen, University of California, Berkeley, 501 Campbell Hall #3411, Berkeley, CA 94720, USA
[4] Columbia Astrophysics Laboratory, Columbia University, 550 West 120th Street, New York, NY 10027, USA
[5] National Radio Astronomy Observatory, P.O. Box O, Socorro, NM 87801, USA
[6] Astrophysics, Department of Physics, University of Oxford, Denys Wilkinson Building, Keble Road, Oxford OX1 3RH, UK
[7] Radboud University, Department of Astrophysics/IMAPP, P.O. Box 9010, 6500 GL Nijmegen, The Netherlands
[8] University of Malta, Institute of Space Sciences and Astronomy, Malta
Received 2025 May 26; revised 2025 December 9; accepted 2026 January 2; published 2026 February 9

Abstract

We report the results of one of the most sensitive pulsar surveys to date targeting the innermost region of the Galactic center (GC) using the Robert C. Byrd Green Bank Telescope at *X* band (8–12 GHz) using data from the Breakthrough Listen initiative. In total, we collected 9.5 hr of data covering the wider ∼8′ diameter of the GC bulge, and 11 hr on the inner 1.′4 region between 2021 May and 2023 December. We conducted a comprehensive Fourier-domain periodicity search targeting both canonical pulsars (CPs) and millisecond pulsars (MSPs), using constant and linearly changing acceleration searches to improve sensitivity to compact binaries. Assuming weak scattering, our searches reached luminosity limits of $L_{\rm min} \approx 0.14$ mJy kpc^2 for CPs and $L_{\rm min} \approx 0.26$ mJy kpc^2 for MSPs—sensitive enough to detect the most luminous pulsars expected in the GC. Among 5282 signal candidates, we identify an interesting 8.19 ms MSP candidate (dispersion measure (DM) of 2775 pc cm^{-3}), persistent in time and frequency across a 1 hr scan at a flux density of $S_{\rm min} \approx 0.007$ mJy. We introduce a novel randomization test for evaluating candidate significance against noise fluctuations, including signal persistence via Kolmogorov–Smirnov tests and flux-versus-DM behavior. We are unable to make a definitive claim about the candidate due to a mixed degree of confidence from these tests and, more broadly, its nondetection in subsequent observations. This deepens the ongoing missing pulsar problem in the GC, reinforcing the idea that strong scattering and/or extreme orbital dynamics may obscure pulsar signals in this region.

Unified Astronomy Thesaurus concepts: Millisecond pulsars (1062); Binary pulsars (153); Radio pulsars (1353); Surveys (1671); Radio telescopes (1360); Radio transient sources (2008); Magnetars (992); Neutron stars (1108); Galactic center (565); Black hole physics (159); Pulsars (1306)

1. Introduction

The Galactic center (GC) hosts the highest number density of stars in the Galaxy (∼10^6 pc^{-3} within 1 pc of Sagittarius A* (Sgr A*); R. Genzel et al. 1996; J.-P. Macquart & N. Kanekar 2015; R. Schödel et al. 2018), and its line of sight offers the largest integrated Galactic star count of any direction in the sky. Therefore, the Breakthrough Listen (BL) initiative is undertaking one of the most extensive and sensitive searches for technosignatures and pulsars directed toward the GC (V. Gajjar et al. 2021). Estimates suggest that approximately 10% of all high-mass stars in the Galaxy reside within ∼200 pc of the GC (D. F. Figer et al. 2004; D. R. Lorimer & M. Kramer 2004; J. S. Deneva et al. 2009), implying a correspondingly large population of neutron stars (NSs) and black holes (BHs). However, despite the expectation of a large population of close-in NSs, no pulsars have been detected within 1 pc of Sgr A* (an angular offset of 25.″2 for $R_0 = 8.18$ kpc), with the exception of the GC magnetar SGR J1745–2900 (2.″4, or <0.1 pc away; R. Eatough et al. 2013a; R. P. Eatough et al. 2013b). The next closest known pulsars remain 12′–18′ away (∼30–40 pc in projection; S. Johnston et al. 2006; J. S. Deneva et al. 2009; M. E. Lower et al. 2024). Nevertheless, indirect observational evidence suggests the presence of NSs near Sgr A*, including dense clusters of young, massive stars (A. M. Ghez et al. 2005), transient sources, which might be low-mass X-ray binaries (M. P. Muno et al. 2005; K. Mori et al. 2021), a possible pulsar wind nebula (Q. D. Wang et al. 2006), radio variables (J.-H. Zhao et al. 2020), and counterparts to sources such as X-ray binaries or unassociated γ rays (M. Ackermann et al. 2017).

Constant star formation and recent starburst models predict 10^2–10^8 NSs in the GC, with 10–10^5 likely to be active pulsars (J. M. Cordes & T. J. W. Lazio 1997; F. Nogueras-Lara et al. 2019). Considering their velocity, lifetime, beaming direction, luminosity, and observational detectability, it is estimated that ∼100–1000 active pulsars could reside in close orbits ($P_b \lesssim 100$ yr) around Sgr A*, with 1–10 of the most luminous potentially detectable by current telescopes (J. M. Cordes & T. J. W. Lazio 1997; P. G. Mezger et al. 1999; E. Pfahl & A. Loeb 2004; J. S. Deneva et al. 2009; R. S. Wharton et al. 2012). This population could also be increased by recycled pulsars originating from binary interactions such as tidal captures and stellar collisions (J. Samsing et al. 2017).

Observing at higher frequencies helps mitigate some observing challenges, namely scattering (a form of temporal smearing due to multipath propagation), which scales as ν^{-4}. Assuming weak scattering, the optimal frequencies for pulsar detection toward the GC are estimated to be up to ∼9 GHz for canonical pulsars (CPs) and ∼22 GHz for millisecond pulsars (MSPs), with an optimal Robert C. Byrd Green Bank Telescope (GBT) survey range of 8–14 GHz (J. M. Cordes & T. J. Lazio 1991; J.-P. Macquart & N. Kanekar 2015; K. M. Rajwade et al. 2017)—a range within which this survey falls.

Discovering a population of pulsars in this region would offer many benefits in probing the GC, including using their age and spin distributions to constrain the past star formation rate (D. R. Lorimer et al. 1993) and gravitational potential in the GC (J. M. Cordes & T. J. W. Lazio 1997). Additionally, pulsars could probe the scattering region around Sgr A*, refining electron density models for the inner Galaxy (J. S. Deneva et al. 2009). Given the extreme stellar density and dynamical environment of the GC, pulsars in exotic configurations—such as pulsar–BH binaries—are also expected to reside there (C.-A. Faucher-Giguère & A. Loeb 2011; V. Gajjar et al. 2021). Perhaps more importantly, discovering and deriving a phase-connected timing solution for a pulsar in a close orbit ($P_b \lesssim 1$ yr) around the supermassive BH (SMBH) Sgr A* would enable measurements of the BH's mass, spin, and quadrupole moment (N. Wex & S. M. Kopeikin 1999; K. Liu et al. 2012, 2014), thereby providing a precise test of the no-hair theorem in general relativity (K. Liu et al. 2012; T. Johannsen 2016; D. Psaltis et al. 2016) for Kerr BHs. Additionally, a pulsar in a very close orbit around Sgr A* ($P_b \lesssim 1$ day) could experience gravitational deflection of its pulses by the SMBH, enabling a probe of the strongly curved spacetime geometry and gravitational field near Sgr A* (Y. Wang et al. 2009a, 2009b; K. Liu et al. 2012; K. Stovall et al. 2012; R. Della Monica et al. 2023).

The lack of CP detections within the innermost 40 pc may indicate an intrinsic deficit, potentially dominated by a magnetar population (J. Dexter & R. M. O'Leary 2014). In the case of MSPs, the dearth may reflect their inherently lower luminosities compared to ordinary pulsars (M. Burgay et al. 2013). Pulsars in the GC are also likely to be more challenging to detect than in typical field surveys due to the region's extreme scattering and complex orbital dynamics. Even in less extreme Galactic environments, marginal candidates have later been confirmed, demonstrating the importance of rigorous candidate vetting in pulsar surveys.

For instance, PSR J2322–2650, a 3.5 ms pulsar discovered in the High Time Resolution Universe (HTRU) survey with an initial signal-to-noise ratio (S/N) ≈12, was confirmed only after follow-up observations with the Lovell Telescope at the Jodrell Bank Observatory, establishing its binary nature (R. Spiewak et al. 2018). Similarly, the coherent reprocessing of the Parkes multibeam pulsar survey (PMPS) data confirmed the intermittent pulsar PSR J1808–1517 (R. P. Eatough et al. 2013c), and the Einstein@Home project uncovered 24 new pulsars missed in original PMPS analysis (B. Knispel et al. 2013). Across past PMPS analyses, many high-quality candidates remain unconfirmed, some of which may be intermittent. More recently, GPU-accelerated coherent reprocessing of HTRU-South Low Latitude survey data recovered dozens of new pulsars by folding candidates to a much lower spectral S/N and exploiting the coherence of folding over the incoherent summing of Fourier components (R. Sengar et al. 2024). Given the profound implications of detecting a short-period MSP orbiting Sgr A*, it is important to examine and follow-up on any low-significance candidates exhibiting pulsarlike properties to determine their true nature, as we have attempted to do in this work.

In this paper, we present results from one of the most sensitive pulsar surveys yet conducted toward the inner 1.′4 (3.33 pc) region of the GC. We also covered the wider ∼8′ diameter of the GC bulge. In Section 2 we detail our observing strategy, data products, and preprocessing techniques, while in Section 3, we describe our periodicity searches employing `PRESTO` acceleration algorithms. In Section 4, we present the results of these searches, including the discovery and characteristics of a particularly intriguing MSP candidate, hereafter referred to as BLPSR. Section 5 rigorously investigates this candidate using novel statistical tests involving data randomization, quantifying the likelihood of its detection occurring by chance. Section 6 analyses our survey sensitivity and compares it with previous pulsar searches in the GC region. We also discuss follow-up observations of BLPSR, examine potential orbital parameters under the assumption that the candidate is genuine, and explore various astrophysical scenarios that might account for its nondetection in subsequent scans. Finally, Section 7 summarizes ongoing and planned future observational efforts.

2. Strategy and Observations

2.1. Observing Strategy

The BL-GC survey is an extensive endeavor to search for radio technosignatures, pulsars, transients, spectral lines, and masers in the GC and neighboring Galactic bulge from 0.7 to 93 GHz (see V. Gajjar et al. 2021, for full survey description). The 0.7–4 GHz component of the survey utilizes the ultrawide band receiver on the Parkes Telescope, while the 4–93 GHz component uses the GBT. As part of this survey, A. Suresh et al. (2022) reported null results from ancillary pulsar searches conducted between 4 and 8 GHz. In this work, we extend the search to the 8–12 GHz GBT *X* band. The GBT *X*-band receiver is a circularly polarized, single beam receiver with a $\theta_{\rm HPBW} = 1.'4$ half-power beamwidth (HPBW) at $\nu_c = 10$ GHz. At this frequency, the GBT's aperture efficiency is 71%, with a beam efficiency of 97%. Unlike traditional single-dish telescopes, the unique off-axis design of the GBT significantly reduces sidelobe contamination,[9] which is especially important in mitigating radio frequency interference (RFI) and identifying real astrophysical signals (see Section 4.1).

We sample an ∼8′ diameter region of the GC and its surroundings with 37 distinct pointings, wherein A00 denotes the GC ($l = 0°$, $b = 0°$) pointing (see Figure 1). The black diamond shows the location of the known GC magnetar, J1745–2900. The cross shows the 4FGL J1745.6–2859 GC source from the fourth Fermi Large Area Telescope (LAT) catalog. The source is ∼ 0.°01 from Sgr A*, and believed to be its γ-ray counterpart (F. Cafardo et al. 2021); it is the only Fermi-LAT catalog source within 4′ of the GC. The 1.28 GHz MeerKAT total intensity mosaic is overlaid in the background to illustrate the GC region covered (I. Heywood et al. 2022).

[9] https://www.gb.nrao.edu/scienceDocs/GBTpg.pdf

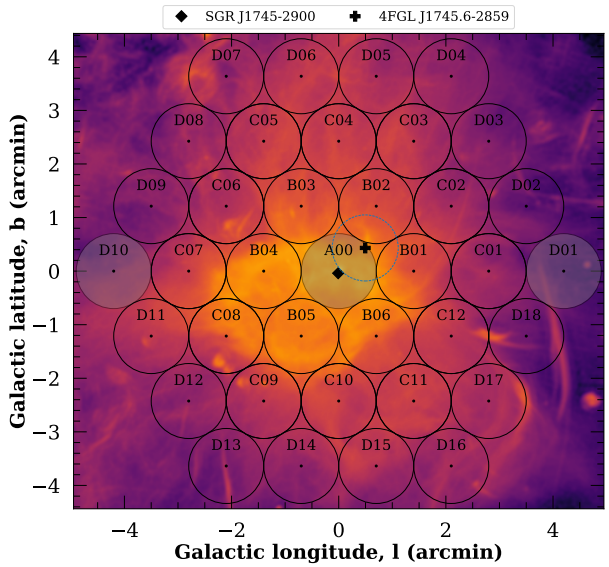

Figure 1. Pointings at GBT *X* band (1.′4 beamwidth) for the BL-GC survey with an overlaid 1.28 GHz MeerKAT total intensity mosaic of the GC (I. Heywood et al. 2022). The central pointing, labeled as A00, indicates the deep pointing of the GC ($l = 0°$, $b = 0°$). The black diamond represents the location of the known GC magnetar, J1745–2900, near the SMBH Sgr A*. The black cross shows the centroid of the 4FGL J1745.6–2859 GC source from the fourth Fermi-LAT catalog, with the dashed blue circle showing its 95% positional uncertainty (a radius of 37″). The rest of the 36 pointings fully sample the wider ∼8′ diameter of the GC bulge region and represent our short 5 minute pointings. The gray-shaded pointings show two separate pairs for our on-off observations, A00–D01 and A00–D10. Due to our odd numbered pointings, A00 is the only pointing which is repeated in a pair. The black points in the center of the beams show the beam centers.

All pointings are arranged in three concentric hexagonal rings, labeled A, B, C, and D, with 1, 6, 12, and 18 pointings per ring, respectively. These pointings were conducted with three short, on-off, 5 minute duration cadences per pointing, for a total of 9.5 hr on target across all pointings. To optimize observing efficiency and reject RFI via position switching, we conducted alternating observations of pairs of pointings. Pointing pairs were chosen such that the beam centers of pairs of pointings were separated by at least $2\theta_{\rm HPBW}$ on the sky (see the gray-shaded pairs A00–D01 and A00–D10 in Figure 1 for example). All other pointing pairs include D03–D18, D02–D17, C01–D16, C02–C11, C03–C12, D05–B01, C04–B06, B02–C10, C05–B05, B03–C09, B04–D13, C08–D15, C07–D14, C06–D12, D08–D11, D06–D09, and D07–D04. Table 1 summarizes all of their coordinates.

We also conducted 11 hr of deep 1 and 2 hr pointings of only the central most region (A00). These observations were conducted over two epochs, 1.5 yr apart. Because interstellar scintillation causes signal intermittency at various timescales depending on the degree of scattering (J. M. Cordes & T. J. Lazio 1991; J. M. Cordes & T. J. W. Lazio 1997), this strategy helps us maximize our chance of detecting narrowband technosignatures (B. Brzycki et al. 2024) and other astrophysical sources such as pulsars that might have lower duty cycles.

2.2. Observations

2.2.1. Short Pointings

We observed the 37 short pointings (see Table 1) from 2021 May 14 to 2022 June 6 with the GBT using the BL digital backend (D. H. E. MacMahon et al. 2018) at *X* band (7.50–11.25 GHz). Each pointing consisted of three 5 minute scans. Baseband voltages were recorded and converted into midtime-resolution total intensity `filterbank` products (8.2 GB per file) to search for CPs. For these midtime-resolution data products, the number of observing channels was 10,240, with a channel bandwidth of 366.21 kHz, and a sampling time of 349.53 μs.

2.2.2. Long Pointings

The 11 hr of deep observations on the A00 pointing were conducted on 2022 June 10 (Epoch 1) and 2023 December 9 (Epoch 2). Table 2 summarizes our long A00 pointing observations, which were conducted over two epochs. The table lists the starting MJD for each scan. Epoch 1 consists of five 1 hr scans (totaling 5 hr, 3.1 TB per scan), and Epoch 2 comprises three 2 hr scans (totaling 6 hr, 8 TB per scan). The increased integration time later adapted during Epoch 2 was to improve our sensitivity. Our observations were constrained to ∼6 hr day^{-1}—the maximum duration the GC remains above the horizon. To verify our data, we recorded a 5 minute scan on test pulsar J1744–1134 during Epoch 1 and on B1929+10 during Epoch 2.

During fall 2023 the GBT *X*-band receiver was replaced with an upgraded instrument, which added an extra 1 GHz of bandwidth, thus covering 7.50–12.38 GHz. Epoch 2 used the upgraded receiver, greatly improving our sensitivity for detecting MSPs in particular. Baseband voltages were recorded and converted into high-time-resolution total intensity `filterbank` products. These 11 hr of observations were used to conduct a deep search for MSPs—an ancillary science goal of the BL-GC survey, which was primarily designed as a technosignature search (V. Gajjar et al. 2021). Hence, for both epochs, we also produced high-time-resolution data products with time and frequency resolutions of 43.69 μs and 91.55 kHz, respectively, resulting in a total of 40,960 frequency channels during Epoch 1 and 53,248 channels during Epoch 2. A detailed summary of the BL reduction pipeline and discussion of various data products is provided by M. Lebofsky et al. (2019).

2.3. Data Preprocessing

All scans were saved and processed on our local workstation (processor model AMD Ryzen Threadripper Pro 5995WX with 64 cores and 128 threads) and standard single-process `PRESTO`[10] (S. M. Ransom 2001) routines were run as outlined below (see Figure 2). We examined our data for narrowband RFI signals using the `rfifind` package with an integration time of 1 s and created an RFI mask for each scan. We find RFI affects ∼1.5% of each short scan and ∼0.03%–0.1% of each long scan, which can be attributed to the low-RFI environment at such high frequencies. This resulted in an effective bandwidth of 3.694 GHz for the short scans, and 3.749 GHz and 4.875 GHz for the long scans from Epochs 1 and 2, respectively. We used the RFI masks with the `prepsubband` package to generate 500 dedispersed time series across 0–5000 pc cm^{-3}, with a dispersion measure (DM) step of 10 pc cm^{-3} using 256 and 4096 subbands for the short and long pointings, respectively. This DM step size was

[10] Available for download from https://github.com/scottransom/presto.

Table 1
Summary of GBT *X*-band Short Observations

Pointing	Date (MJD)	R.A. (J2000) (HH:MM:SS.SS)	Decl. (J2000) (DD:MM:SS.SS)	l (deg)	b (deg)	Total exp.[a] (hr)	No. of candidates[b]
Short Pointings							
A00[c]	59348.258	17:45:40.04	−29:00:28.10	359.944	−0.046	0.5	26
B01	59348.412	17:45:43.38	−28:59:16.40	359.968	−0.046	0.25	5
B02	59736.187	17:45:36.98	−28:59:14.35	359.956	−0.026	0.25	7
B03	59736.231	17:45:33.64	−29:00:26.04	359.933	−0.026	0.25	20
B04	59736.252	17:45:36.70	−29:01:39.80	359.921	−0.046	0.25	20
B05	59736.212	17:45:43.11	−29:01:41.85	359.933	−0.066	0.25	11
B06	59348.412	17:45:46.44	−29:00:30.14	359.956	−0.066	0.25	9
C01	59348.344	17:45:46.71	−28:58:04.69	359.991	−0.046	0.25	5
C02	59348.366	17:45:40.31	−28:58:02.65	359.979	−0.026	0.25	8
C03	59348.387	17:45:33.91	−28:58:00.60	359.968	−0.006	0.25	8
C04	59348.430	17:45:30.57	−28:59:12.29	359.944	−0.006	0.25	6
C05	59736.209	17:45:27.24	−29:00:23.97	359.921	−0.006	0.25	10
C06	59736.317	17:45:30.30	−29:01:37.73	359.909	−0.026	0.25	16
C07	59736.295	17:45:33.37	−29:02:51.49	359.898	−0.046	0.25	16
C08	59736.274	17:45:39.77	−29:02:53.55	359.9909	−0.066	0.25	5
C09	59736.234	17:45:46.17	−29:02:55.59	359.921	−0.087	0.25	6
C10	59736.191	17:45:49.51	−29:01:43.87	359.944	−0.087	0.25	8
C11	59348.369	17:45:52.84	−29:00:32.15	359.968	−0.087	0.25	7
C12	59348.391	17:45:49.78	−28:59:18.42	359.979	−0.066	0.25	8
D01	59348.283	17:45:50.04	−28:56:52.97	0.014	−0.046	0.25	7
D02	59348.323	17:45:43.64	−28:56:50.95	0.003	−0.026	0.25	4
D03	59348.301	17:45:37.25	−28:56:48.90	359.991	−0.006	0.25	10
D04	59736.385	17:45:30.85	−28:56:46.84	359.979	0.014	0.25	28
D05	59348.409	17:45:27.51	−28:57:58.52	359.956	0.014	0.25	9
D06	59736.360	17:45:24.18	−28:59:10.20	359.933	0.014	0.25	26
D07	59736.381	17:45:20.84	−29:00:21.88	359.909	0.014	0.25	17
D08	59736.338	17:45:23.90	−29:01:35.65	359.898	−0.006	0.25	24
D09	59736.363	17:45:26.96	−29:02:49.42	359.886	−0.026	0.25	20
D10	59348.262	17:45:30.03	−29:04:03.18	359.874	−0.046	0.25	16
D11	59736.342	17:45:36.43	−29:04:05.25	359.886	−0.066	0.25	9
D12	59736.320	17:45:42.84	−29:04:07.29	359.898	−0.087	0.25	11
D13	59736.256	17:45:49.24	−29:04:09.32	359.909	−0.107	0.25	17
D14	59736.299	17:45:52.58	−29:02:57.60	359.933	−0.107	0.25	13
D15	59736.277	17:45:55.91	−29:01:45.88	359.956	−0.107	0.25	18
D16	59348.348	17:45:59.24	−29:00:34.15	359.979	−0.107	0.25	6
D17	59348.326	17:45:56.18	−28:59:20.43	359.991	−0.087	0.25	12
D18	59348.305	17:45:53.11	−28:58:06.70	0.003	−0.066	0.25	7

Notes.
[a] Each pointing was observed for 15 minutes, split into three 5 minute scans, alternating between pairs of pointings as part of the technosignature survey strategy (see Section 2.1).
[b] Number of candidate signals detected per pointing for $z_{\max} = 0$.
[c] The A00 short pointing was observed for 30 minutes due to it being part of two pairs of pointings.

chosen using the `DDplan.py` code to optimize the sensitivity of pulsar searching. We opted for 4096 subbands for the long pointings to minimize the time delay smearing caused by the frequency dependence of radio waves in the interstellar plasma and thereby ensure a thorough search for candidates. Using subbandwidths of 0.92 MHz for Epoch 1 and 1.19 MHz for Epoch 2, we calculated negligible dispersive delays of 16 μs and 18 μs per subband, respectively. To reduce computational cost while retaining sensitivity, we also downsampled by a factor of 4.

We then applied a fast Fourier transform to each dedispersed time series with the `realfft` package. To reduce the effects of red noise and help flatten the power spectrum, we applied the `rednoise` routine to each spectra by subtracting the low-frequency noise baseline. This involves measuring the median power in blocks of Fourier frequency bins and scaling it by log2, which converts it to an equivalent mean power, assuming exponential noise distribution. The block size increases with frequency using adaptive windowing, starting with 6 bins at low frequencies (`-startwidth = 6`) and growing to 100 bins (`-endwidth = 100`) by 6 Hz (`-endfreq = 6`). For frequencies above 6 Hz where the spectrum flattens, the block size remains fixed at 100 bins (S. Ransom 2011; P. Lazarus et al. 2015; P. Torne et al. 2021; A. Suresh et al. 2022). After dedispersing, the data was barycentered to remove the effects from the rotation of the Earth and its motion around the Sun.

3. Periodicity Searches

Detecting pulsars in binary systems, especially those orbiting compact, massive objects such as Sgr A*, is

Table 2
Summary of GBT *X*-band Long Observations

Epoch	Scan[a]	Date (MJD)	No. of Candidates		
			$z_{\max} = 0$	$z_{\max} = 200$	$z_{\max} = 200$, $w_{\max} = 600$
1	1.1	59740.146	13	24	97
	1.2	59740.188	18	30	81
	1.3	59740.230	11	35	79
	1.4	59740.272	14	26	75
	1.5	59740.313	14	38	111
2	2.1	60287.632	44	106	324
	2.1.1	⋯	59	54	117
	2.1.2	⋯	20	126	207
	2.2	60287.715	41	69	257
	2.2.1	⋯	38	56	120
	2.2.2	⋯	28	67	209
	2.3	60287.799	68	112	517
	2.3.1	⋯	68	107	386
	2.3.2	⋯	46	200	715

Note.
[a] For Epoch 2, labels "2.n.1" and "2.n.2" indicate the first and second halves of the 2 hr integrations, respectively, with each treated as a separate 1 hr segment.

challenging due to the binary orbital motion and acceleration of the pulsar. This introduces a time-dependent Doppler drift, which causes the apparent pulsar spin frequency to change with time, causing the signal harmonics to smear across neighboring frequency bins in the power spectrum. Fourier-domain acceleration searches account for this smearing by assuming a constant (z for $T \lesssim P_b/10$) or linearly evolving "jerk" (w for $T \lesssim P_b/15$) line-of-sight pulsar acceleration, where z and w correspond to the number of Fourier frequency (and frequency derivative, respectively) bins that the signal drifts through in an observation (S. M. Ransom 2001; B. C. Andersen & S. M. Ransom 2018). The parameters $z_{\max}$ and $w_{\max}$ define the maximum number of bins over which a signal can still be recovered in the search. This makes our periodicity search particularly sensitive to highly accelerated pulsars that may be directly orbiting Sgr A* and/or stellar-mass BHs, as well as other standard known compact binary configurations.

3.1. Acceleration Searches

We conducted blind searches for isolated and binary pulsars in the frequency range 0.01–10,000 Hz, sampling a 5D parameter space of DM, f (spin frequency), N_h (number of harmonics), $z_{\max}$, and $w_{\max}$. Our search encompassed both CPs and MSPs, as our detection threshold is sensitive to a wide range of spin periods, including hundreds of slow pulsars and at least a few MSPs based on our sensitivity calculations for the known pulsar population (see Section 6.2 for details) We adopt the recommended values of $z_{\max} = 200$ and $w_{\max} = 600$ from B. C. Andersen & S. M. Ransom (2018).

To determine the detectability of pulsars in compact orbits in our survey, we used the line-of-sight pulsar acceleration (a_l) and jerk (j_l) equations (M. Bagchi et al. 2013; K. Liu et al. 2021)

$$a_l = -\left(\frac{2\pi}{P_b}\right)^2 \frac{a_p \sin i}{(1-e^2)^2}(1 + e\cos A_T)^2 \sin(A_T + \omega), \quad (1)$$

and

$$j_l = -\left(\frac{2\pi}{P_b}\right)^3 \frac{a_p \sin i}{(1-e^2)^{7/2}}(1 + e\cos A_T)^3 \times [e\cos\omega + \cos(A_T + \omega) - 3e\sin(A_T + \omega)\sin A_T], \quad (2)$$

where e is the orbital eccentricity, P_b is the orbital period, a_p is the semimajor axis, i is the orbital inclination, ω is the argument of periapsis, and A_T is the true anomaly. We also use the corresponding Fourier-domain drift equations for acceleration and jerk (S. M. Ransom 2001; B. C. Andersen & S. M. Ransom 2018):

$$z = h\left(\frac{a_l f T^2}{c}\right), \quad (3)$$

and

$$w = h\left(\frac{j_l f T^3}{c}\right), \quad (4)$$

where h is the harmonic number (with $h = 1$ being the fundamental frequency), f is the pulsar spin frequency, c is the speed of light in a vacuum, and T the length of the observation.

We considered an $M_p = 2.14\,M_\odot$ pulsar—the highest measured NS mass to date (H. T. Cromartie et al. 2020)—in an edge-on orbit (inclination $i = 90°$). To estimate the maximum Fourier-domain drift, we evaluated a_l at $A_T = 0°$ and $\omega = \pi/2$, which together maximize the projected acceleration. For jerk, we kept $A_T = 0°$ and instead set $\omega = 0°$, which maximizes the projected jerk. This 90° phase shift arises from the analytic dependence on the $\sin(A_T + \omega)$ and $\cos(A_T + \omega)$ terms in Equations (1) and (2), and corresponds to a shift of 90° in the projected orbital phase. We used our 1 and 2 hr integration times and applied Kepler's third law to solve for a_p, then substituted the resulting expressions into Equations (3) and (4), yielding $z(A_T, \omega)$ and $w(A_T, \omega)$. Applying $A_T = 0°$ and $\omega = \pi/2$

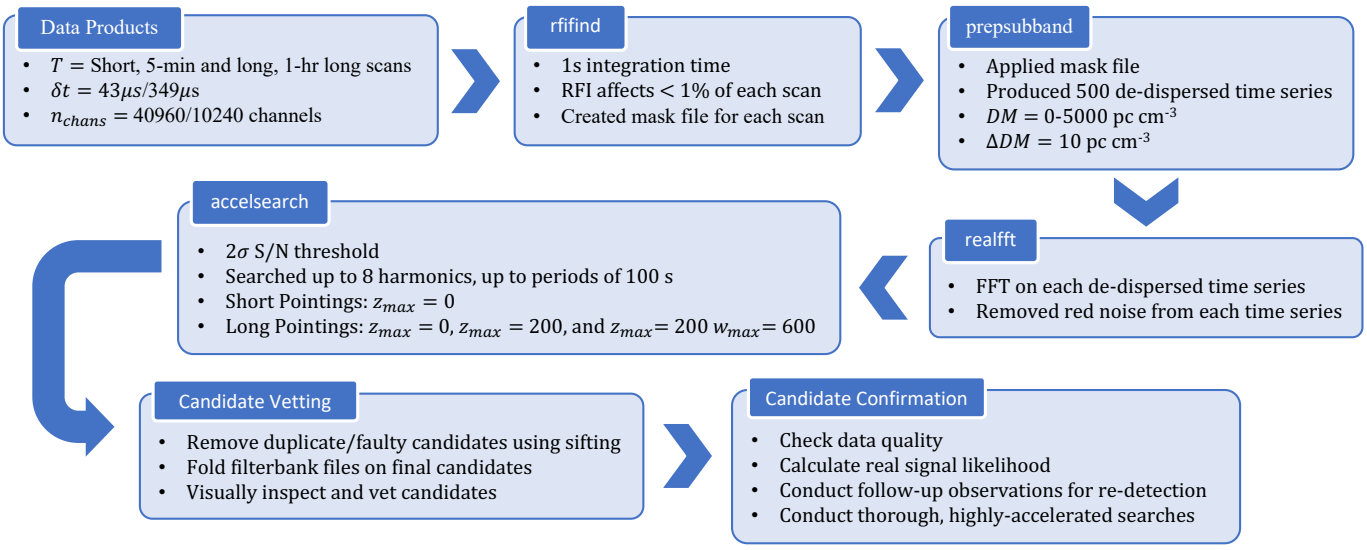

Figure 2. Flowchart of PRESTO commands run for our survey search.

for z and $\omega = 0°$ for w yields

$$z(0°, \pi/2) = h\frac{G^{1/3}}{c\,(4\pi^2)^{2/3}}\frac{(M_c + M_p)^{1/3}(1+e)^2\,T^2}{P_0\,P_b^{4/3}(1-e^2)^2}, \quad (5)$$

and

$$w(0°, 0°) = h\frac{8\,\pi^3\,G^{1/3}}{c\,(4\pi^2)^{1/3}}\frac{(M_c + M_p)^{1/3}(1+e)^4\,T^3}{P_0\,P_b^{7/3}(1-e^2)^{7/2}}, \quad (6)$$

where M_c is the mass of the binary companion and P_0 is the intrinsic pulsar spin period. We sampled parameter grids of $P_b \in [1, 1\times10^5]$ hr and $e \in [0.0, 0.8]$, assuming a $P_0 = 10$ ms pulsar in orbit around either the SMBH Sgr A* ($M_{\mathrm{Sgr\,A*}} = 4.30\times10^6\,M_\odot$), a stellar-mass BH ($M_{\mathrm{BH}} = 9\,M_\odot$), or a 0.1 $M_\odot$ companion —the latter being most representative of typical MSP companions. To reflect the conditions of our search pipeline, we used $h = 8$, consistent with the harmonic summing used in our Fourier-domain searches. Higher harmonic summing improves sensitivity to pulsars with narrower duty cycles (S. M. Ransom et al. 2002) and those in larger orbits with small accelerations. For each (e, M_c) combination, we determined the shortest P_b such that the projected acceleration and jerk remain at or below our thresholds, satisfying $z(0°, \pi/2) = 200$ and $w(0°, 0°) = 600$. This $P_{b,\mathrm{min}}$ defines the shortest orbital period for which a system would remain detectable at all orbital phases within our search limits. More compact binaries (with shorter P_b) can exceed $z = 200$ and/or $w = 600$ at other orbital phases, but may still be detectable by our search if observed near favorable phases. However, because our search aims to be phase independent, we define our recoverability conservatively, requiring detectability at all orbital phases, and adopt the maximum projected acceleration and jerk values in Equations (5) and (6) to set $P_{b,\mathrm{min}}$ limits.

Figure 3 shows the resulting contours of constant absolute z_{max} (solid lines) and w_{max} (dashed lines) for both integration times (1 (black) and 2 hr (blue)) under the three binary scenarios: a pulsar orbiting Sgr A* (Figure 3(a)), a stellar-mass BH (Figure 3(b)), and a 0.1 $M_\odot$ companion (Figure 3(c)). These contours, plotted in the (e, P_b) plane, represent the $P_{b,\mathrm{min}}$ accessible to our search at each e, assuming full orbital phase coverage, and search limits of $z_{\mathrm{max}} = 200$ and $w_{\mathrm{max}} = 600$ (see Section 3.1.2, where $w_{\mathrm{max}} = 600$ includes $z_{\mathrm{max}} = 200$). Systems lying above the contours (i.e., wider orbits at the same e) produce lower maximum projected acceleration and jerk ($z < 200$ and $w < 600$) and are therefore fully detectable by our search at all orbital phases. In contrast, systems below the contours (i.e., more compact orbits at the same e), would either (i) require a more sensitive search with higher acceleration and/or jerk limits, or (ii) be detectable only when observed near favorable orbital phases. This behavior holds for all eccentricities. As e increases, z and w become more extreme, shifting the $P_{b,\mathrm{min}}$ contours upward. That is, more eccentric systems require longer orbital periods to remain detectable within our limits.

In the Sgr A* case, our search of $z_{\mathrm{max}} = 200$ allows detection of orbital periods down to $P_{b,\mathrm{min}} \sim 0.7$ yr for $e \sim 0.5$, and ~0.3 yr for $e \sim 0.1$, assuming detectability at all orbital phases. Jerk searches with $w_{\mathrm{max}} = 600$ extend this coverage down to ~15 days and ~6 days, respectively. For a 9 $M_\odot$ BH companion, the $z_{\mathrm{max}} = 200$ reaches down to $P_{b,\mathrm{min}} \sim 11$ days for $e \sim 0.5$, and ~4 days for $e \sim 0.1$. Jerk searches extend this to $P_{b,\mathrm{min}} \sim 2$ days and ~22 hr, respectively. Finally, for the 0.1 $M_\odot$ companion case, $z_{\mathrm{max}} = 200$ allows detection down to $P_{b,\mathrm{min}} \sim 7$ days for $e \sim 0.5$, and ~3 days for $e \sim 0.1$. Jerk $w_{\mathrm{max}} = 600$ searches extend these limits to $P_{b,\mathrm{min}} \sim 1.9$ days and ~17 hr, respectively. These estimates are consistent with those reported in R. P. Eatough et al. (2021) and K. Liu et al. (2021). Although more computationally expensive, jerk searches significantly extend orbital coverage to pulsars in highly compact orbits, such as those orbiting Sgr A*, relativistic double-NS systems, or systems with high eccentricities, which would otherwise require values much larger than $z_{\mathrm{max}} = 200$ to detect. This is evident from the 1–2 order of magnitude improvement in the $P_{b,\mathrm{min}}$ shown in Figure 3.

It is also evident from Figure 3 that, as the assumed companion mass decreases, the search becomes limited by the absolute minimum P_b detectable given our integration times. This is indicated by the onset of the shaded black and blue exclusion regions. These detection constraints arise from the condition of $T \lesssim 0.10 P_b$ for constant acceleration searches, which limits our parameter range to orbits with $P_b \gtrsim 10$ hr for

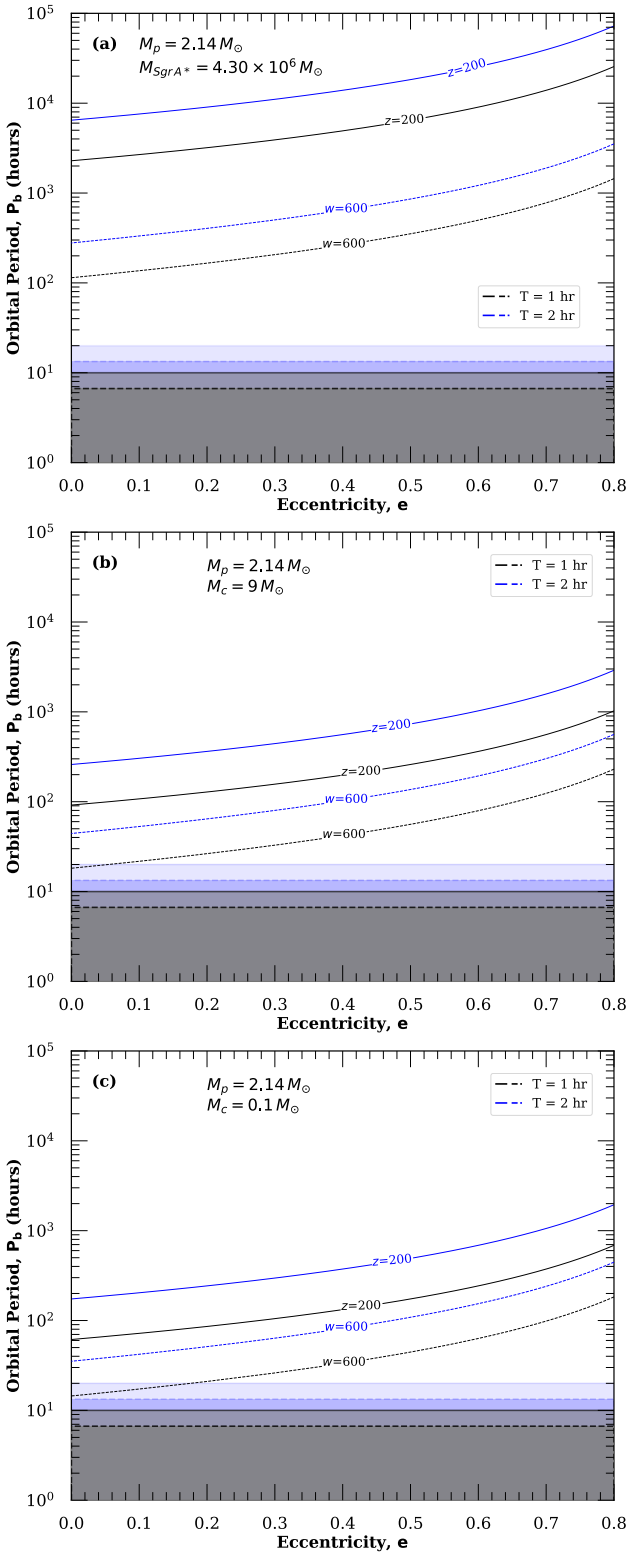

Figure 3. Contours of maximum Fourier-domain drift for a 10 ms pulsar with $h = 8$ harmonics, sampled over orbital period and eccentricity. Panels shows a pulsar orbiting:(a) the GC SMBH, (b) a 9 $M_\odot$ BH, and (c) a 0.1 $M_\odot$ companion. Solid and dashed lines correspond to constant (z) and linearly changing (w) acceleration thresholds, respectively. Black and blue lines show results for 1 and 2 hr integrations, respectively. Shaded regions indicate the absolute minimum P_b detectable given our integration times.

the 1 hr integrations and $P_b \gtrsim 20$ hr for the 2 hr integrations (B. C. Andersen & S. M. Ransom 2018). Likewise, for jerk searches, the condition $T \lesssim 0.15 P_b$ restricts detections to $P_b \gtrsim 6.67$ hr and $P_b \gtrsim 13.33$ hr for each integration time, respectively (B. C. Andersen & S. M. Ransom 2018). We note that these threshold rules are based on the assumption of a solar-mass companion. In systems with more massive companions—such as a stellar-mass BH or SMBH—the orbital phases over which a signal is detectable are reduced due to the rapid variations in line-of-sight accelerations and jerk. This effect has been demonstrated in K. Liu et al. (2014). While shorter integrations can mitigate this partially, high eccentricities may still prevent detection, particularly near periastron where acceleration changes the most rapidly.

3.1.1. Short Pointings

Given the short 5 minute duration of these pointings, we performed a blind, zero-acceleration search ($z_{\max} = 0$) using `accelsearch` on all 37 short pointings to target isolated NSs. Given the short integrations and zero acceleration, we conducted the searches using the local workstation, with each scan taking $\sim$1 minute. With a cadence of six per pair, we analyzed a total of 114 midtime-resolution `filterbank` files, applying a 2σ detection threshold on the harmonic-summed power spectra. Note that σ here includes a correction for the number of independent frequencies and derivatives searched in each run (S. M. Ransom 2001). Periods were searched up to eight harmonics, after which the `sifting` algorithm was used to group hits in adjacent trial DMs and frequencies f into distinct candidates, while removing any duplicate candidates across DM, P, $\dot{P}$, and harmonics. `sifting` yields single-trial significance values, σ_{ps}, which are interpreted as the equivalent Gaussian significance of a frequency f in the χ^2-distributed power spectrum (assuming a dereddened, Gaussian white-noise background). This allows for a direct comparison of candidates across different searches. Final candidates were folded on the raw `filterbank` files for visual inspection using `prepfold`. Folding was performed on the local workstation utilizing parallelization, with each fold requiring $\sim$10 minutes.

3.1.2. Long Pointings

We conducted two constant acceleration searches ($z_{\max} = 0$ and $z_{\max} = 200$) and one linearly changing acceleration (jerk) search ($z_{\max} = 200$ and $w_{\max} = 600$) on Epochs 1 and 2, which comprised five 1 hr and three 2 hr high-time-resolution `filterbank` files. Due to the computational intensity involved, we executed `accelsearch` on Columbia University's High-Performance Computing (HPC) cluster, equipped with Dual Intel Xeon Gold 6226R processors across 286 nodes (32 cores per node). We modified our analysis pipeline to run these searches in parallel—50 dedispersed time series simultaneously—to optimize runtime. Memory allocation was set at 8 GB per core for constant acceleration searches and 16 GB per core for the jerk searches. Typical run times were approximately 10 minutes per search for $z_{\max} = 0$, 30 minutes for $z_{\max} = 200$, and $\approx$1 day for the jerk search ($z_{\max} = 200$ and $w_{\max} = 600$). Given our large number of dedispersed time series (500), utilizing parallelization was essential. We again applied a 2σ threshold to ensure that no potential candidates were overlooked. Additionally, since shorter integration times improve sensitivity to a broader range of orbital periods (see Figure 3), we also divided the 2 hr integrations into 1 hr segments to maximize our detection

capability. Such a comprehensive approach is especially important given the poorly understood electron density environment in the GC and the uncertainties in the location, uniformity, and/or patchiness of the scattering screen—all of which can contribute to signal intermittency. Additional factors such as binary eclipses may also obscure pulsar signals at certain orbital phases (K. I. Perez et al. 2023).

Like the short pointings, periods were searched up to eight harmonics, and candidates were grouped using the `sifting` routine, resulting in $\sigma_{ps,\min} = 6$ as the final detection threshold for comparison. The parameters from the blind searches were then used to fold the remaining candidates on the raw `filterbank` files for visual inspection using `prepfold`. Folding was performed on the HPC cluster, as each 1 hr observation required 1 day of folding per candidate. To expedite the analysis for all candidates, we also parallelized the folding tasks across multiple compute nodes.

4. Results

4.1. Short Pointings

Across all 37 short, 5 minute pointings, we detected a total of 455 signal candidates, including some of which were duplicated across multiple pointings. Table 1 summarizes the number of candidates detected per pointing. To mitigate false positives, we used a position-switching strategy (see Section 2.1). This allowed us to reject 11 of these 455 candidates, as these signals were detected in paired pointings separated by more than two beamwidths—behavior indicative of terrestrial RFI. Some of these signals also exhibited low DMs, high duty cycles, and/or were only present in a few time samples.

To further vet our candidates, we implemented a second filter to determine potential sidelobe contamination. Although sidelobe effects are generally minimal with the GBT, we adopted a conservative approach by cross checking for each of the remaining 444 candidates beyond their adjacent pointings. Based on GBT measurements at *X* band—where the first sidelobe is ~ -27 dB below the main lobe (D. T. Frayer 2017)—we estimate that the first sidelobe occurs at an angle of $\approx 1\farcm86$ away from the main lobe (over a beamwidth away), meaning that any candidate detected in directly adjacent pointings is likely a sidelobe artifact. Similarly, the second sidelobe, with an estimated power level of ~ -29 dB, is expected at an angle of $\sim 2\farcm76$ away from the main lobe (two beamwidths away).

A candidate was flagged for sidelobe contamination if it appeared in multiple pointings. To distinguish a true detection from RFI, we utilized a beam adjacency mapping, assigning each beam to its immediate neighbors (e.g., beam A00 maps to beams B01–B06). Candidates appearing in nonadjacent beams were classified as RFI and removed from further analysis, since signals detected two beamwidths away are almost certainly spurious. Ultimately, we rejected all 444 candidates, i.e., no pulsars were detected. Additionally, a visual inspection of all 455 candidates revealed time and frequency features not characteristic of a typical pulsar (large duty cycles, non-persistent signal, and a reduced χ^2 decreasing or staying constant), further confirming their classification as RFI. This RFI behavior is consistent with that observed in the GC survey at *C* band (4–8 GHz) for the short pointings surrounding A00 (A. Suresh et al. 2022), where the lower frequencies led to a higher false-positive rate, highlighting the advantages of higher-frequency surveys of the GC.

4.2. Long Pointings

We detected a total of 4827 periodicity candidates across both epochs. Table 2 shows the number of candidates detected in each acceleration search per scan. For Epoch 2, labels "2.n.1" and "2.n.2" indicate the first and second halves of the 2 hr integrations, respectively, with each treated as a separate 1 hr segment. Duplicate candidates within a single scan (e.g., those detected in both the $z_{\max} = 0$ and $z_{\max} = 200$ searches) were counted only once; however, some candidates in Epoch 2 may have been recorded twice if they were detected in both the full 2 hr integration and in the split 1 hr segments. Using the full 2 hr integrations is especially advantageous for detecting extremely dim pulsars (see Section 6.2 for more details). As expected, the number of detections increases with integration time: from Equations (3) and (4), both the z and w bins scale with the square or cube of the scan integration time, so longer scans and higher bin values yield more candidates.

Figures 4 and 5 present the statistical distributions of DM, period, and σ_{ps} for the 3289 candidates detected in the 1 hr integrations, with a median of $\tilde{x}_{\rm DM} = 1830$ pc cm^{-3}, $\tilde{x}_P = 13.4$ ms, and $\tilde{x}_{\sigma_{ps}} = 7.7$. We see candidates span a wide range of periods, from millisecond to subsecond scales, revealing a mix of potential pulsars and interference. However, the majority fall between $P \in [1,\ 100]$ ms, indicating a statistical sampling effect and periodic RFI. To maintain consistency across epochs, candidates from the full 2 hr integrations are excluded from these plots (though they are reported in Table 2 for completeness). Candidates are distinguished by acceleration search parameters: dots represent $z_{\max} = 0$, crosses denote $z_{\max} = 200$, and squares indicate $z_{\max} = 200$ and $w_{\max} = 600$; candidates from Epoch 1 are shown in green and those from Epoch 2 in orange. The red diamond, denoted as the BLPSR, marks an interesting 8.19 ms MSP candidate found in our searches and will be discussed in detail in the following subsection.

Figure 4 displays the DM–period distribution for our candidate detections, with the inset zooming into the 8–8.5 ms period range to highlight the location of BLPSR relative to other candidates, including the signal associated with the 60 Hz power line (dashed black line). We observe a cluster of candidates in Epoch 2 with DMs between 0–200 pc cm^{-3}. This epoch yielded more candidates overall, likely attributable to the wider bandwidth and hence increased sensitivity to RFI. There was also an increased incidence of detections toward the end of the session (second half of the last scan) as the GC approached the horizon, leading to increased interference at lower DMs. A spike in candidates at DM $\approx$ 2250–2300 was also identified, driven by two strong narrowband RFI signals and their harmonics; these alone accounted for $\approx$80% of candidates in that DM range across all acceleration searches in the second half of the final scan.

Figure 5 shows the σ_{ps}–period distribution, where the majority of candidates have $\sigma_{ps} < 10$. Although pulsars near the GC are expected to be faint (and hence have a low σ_{ps}), RFI is also a culprit, with very strong RFI producing higher σ_{ps}. Similar to the short pointings, many more false positives were found for the long 6 hr A00 pointings at *C* band (A. Suresh et al. 2022) than at *X* band, again showing the importance of conducting higher-frequency pulsar surveys of

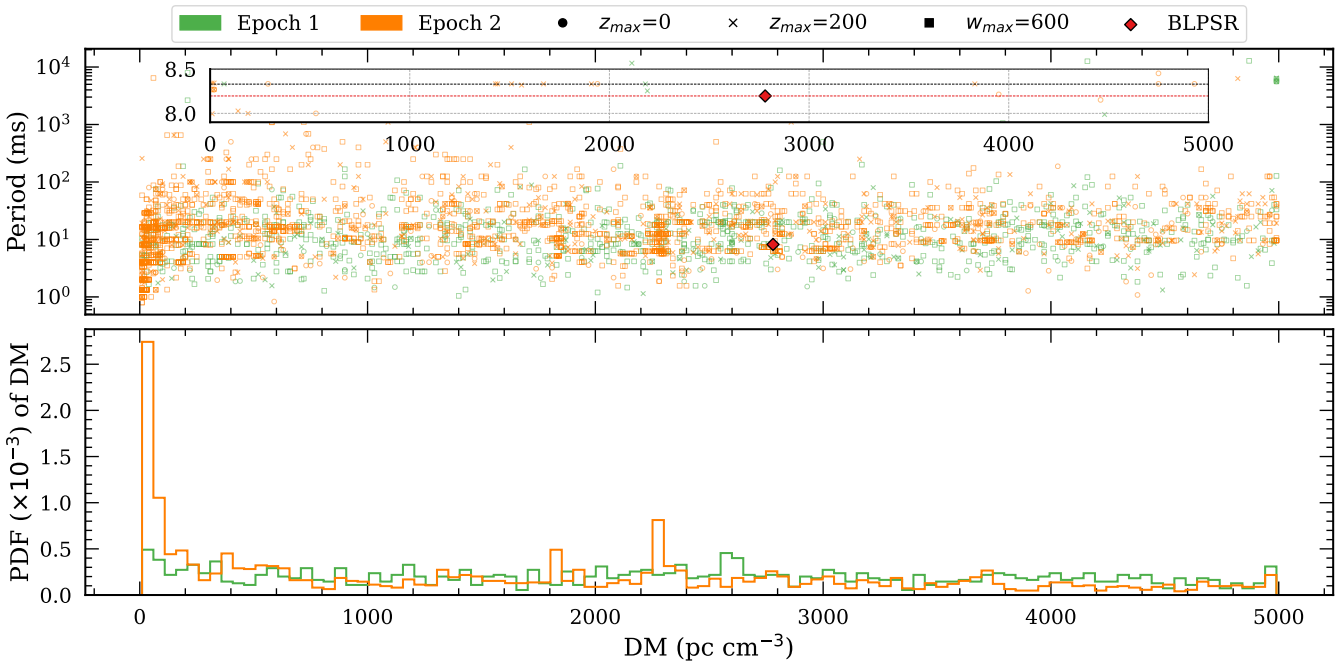

Figure 4. Top panel: period vs. DM for all candidates detected blindly at all three of our accelerated searches $z_{\max} = 0$ (circles), $z_{\max} = 200$ (crosses), and $z_{\max} = 200$ and $w_{\max} = 600$ (squares) across both epochs, using 4096 subbands. The BLPSR candidate is marked by the red diamond, and each epoch is color coded accordingly. The inset plot provides a zoomed-in view of candidates near BLPSR. The red dashed line indicates BLPSR's period (8.19 ms), with no other candidate matching this value. The black dashed line marks a recurring 8.33 ms candidate, corresponding to twice the frequency of 60 Hz power lines. Bottom panel: probability distribution function (PDF) of candidate DMs binned uniformly to 50 pc cm^{-3} resolution, per epoch.

the GC. Following visual inspection of all 4827 candidates, all were classified as RFI. Although several pulsarlike profiles were detected at different periods, they all showed a reduced χ^2 peak near DM = 0 pc cm^{-3} and exhibited no broadband properties. A single outlier—the BLPSR candidate—stood out and warranted closer examination.

4.3. BLPSR Candidate

The MSP candidate, BLPSR, was detected during our $z_{\max} = 200$ acceleration searches with a period of $P = 8.19$ ms in the first 1 hr scan of Epoch 1 (Scan 1.1) during the long-pointing observations of A00. It was detected at a DM of 2780 pc cm^{-3}, $\sigma_{ps} = 7.28$, $z = 2.75$, and $w = 0$, with a $\dot{P} = -1.23 \times 10^{-11}$ s s^{-1} corresponding to a line-of-sight acceleration of $a_l = -0.45$ m s^{-2}, where a negative a_l is defined as accelerating toward the observer. Although its DM is substantially higher than that of the nearest known NS to the GC—magnetar PSR J1745–2900 (DM = 1778 pc cm^{-3})—it is consistent with expectations for sources located in the inner regions of the GC, given the distance uncertainty of the patchy scattering screen (see Section 6.5 for further discussion). Applying the NE2001 Galactic electron density model using `PyGEDM` predicts a distance of $d_{\rm NE2001} = 8.59$ kpc (J. M. Cordes & T. J. W. Lazio 2003; D. C. Price et al. 2021), supporting the candidate's location near Sgr A*.

BLPSR was initially selected based on its detection significance ($>6\sigma_{ps}$), coherent power, and its temporal and spectral characteristics after folding. Its centroid—the signal's approximate location in the normalized time series—is 0.476 at the fundamental frequency. Similarly, its purity—a measure of the rms dispersion of the pulsations in time with respect to the centroid—is 0.899. This indicates that the signal is present throughout nearly the entire scan, supporting a real, temporally stable signal. As seen in Figure 6, the signal persists for a large fraction of the entire 1 hr integration and appears present across most of the band in the dynamic spectrum. The integrated profile's reduced χ^2 increases over time, as does the reduced χ^2 as a function of P and $\dot{P}$. However, we also observe variations in signal intensity across both time and frequency, which may result from a lower S/N and/or complex propagation effects in the interstellar medium. While the NE2001 model (J. M. Cordes & T. J. W. Lazio 2003) predicts strong scattering ($\tau_{ss} = 2000\nu^{-4}$ s), corresponding to pulse a broadening of ∼0.2 s at X band ($\nu_c = 10$ GHz), the weak-scattering scenario observed for the GC magnetar PSR J1745–2900 (L. G. Spitler et al. 2014), with $\tau_{ws} = 1.3\,\nu^{-4}$ s, would produce negligible pulse broadening of ≈130 μs for our putative BLPSR candidate. We attempted to measure the scintillation timescale using the autocorrelation function of the on-pulse intensity over time, and found a pulse intensity scintillation timescale of ∼1800 s. This timescale is inconsistent with the expected longer timescales of diffractive scintillation at this frequency. Thus, neither pulse broadening nor scintillation appears to account for the observed short-timescale variability.

In the broader candidate population, BLPSR was notable despite being centrally located in the σ_{ps}–period distribution cluster (see Figure 5). Specifically, it is the only candidate detected at its specific period (see Figure 4). Modified z scores (standard deviations from the median) for DM, P, and σ_{ps} based on the long-pointing candidate distributions in Figures 4 and 5 yield $z_{\rm DM} = 0.48$, $z_P = -0.49$, and $z_{\sigma_{ps}} = -0.3$. Although these indicate that BLPSR is not an outlier among the 4827 detected candidates, visual inspection revealed it to be the only one with pulsarlike properties, requiring further examination. BLPSR also exhibited the highest coherent power (253.5; marked by a red diamond in Figure 7(a)) among all candidates detected at $z_{\max} = 200$ during Epoch 1,

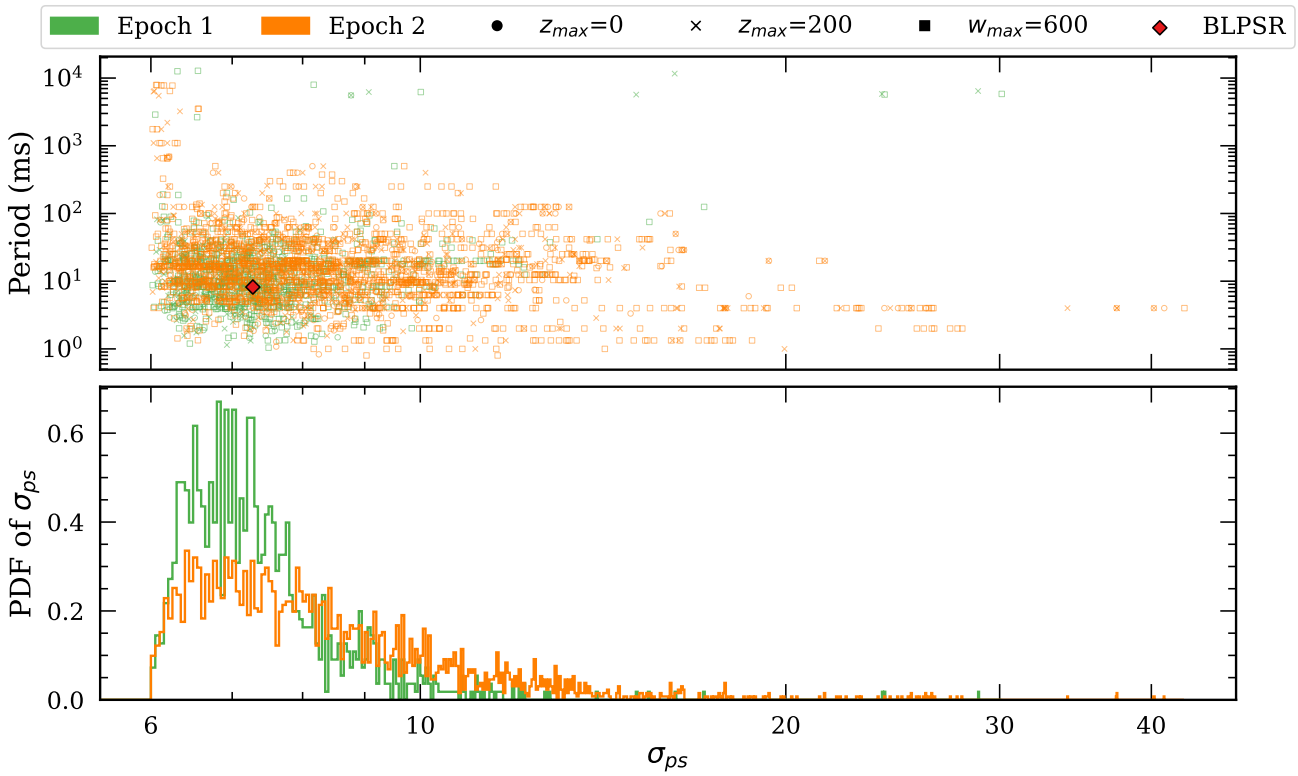

Figure 5. Top panel: period vs. σ_{ps} for all candidates detected blindly at all three of our accelerated searches $z_{\max} = 0$ (circles), $z_{\max} = 200$ (crosses), and $z_{\max} = 200$ and $w_{\max} = 600$ (squares) across both epochs, using 4096 subbands. The BLPSR candidate is marked by the red diamond, and each epoch is color coded accordingly. Bottom panel: PDF of equivalent Gaussian significance (σ_{ps}) of candidates in power spectra binned uniformly to ln σ_{ps} with width ≈ 0.05, per epoch.

with a z score of $z_{\text{power}} = 7.84$, showing that BLPSR is an outlier when considering this parameter. We also computed the total coherent power of BLPSR's eight harmonics by iteratively summing their respective complex Fourier amplitudes and phases, demonstrating how the signal power amplifies with each harmonic step, as expected for a true pulsar signal (see Figure 7(b)).[11]

Although the detection Gaussian significance of BLPSR is not particularly high, we chose to examine BLPSR closely due to the importance of finding pulsars near the GC and minimizing the false-negative rate. Specifically, we deliberately examined candidates with lower folded profile reduced χ^2 values, among which BLPSR emerged. If we had imposed a stricter detection threshold (e.g., S/N > 5), BLPSR would not have been flagged for visual inspection. Although BLPSR did cross our detection threshold, it is still near the border line and could not be categorically ruled out as a signal originating from either RFI or noise fluctuations. The following section aims to qualitatively examine BLPSR—representing one of the most detailed inspections carried out on any potential pulsar candidate from a single-dish telescope to date.

5. Examination of BLPSR Detection Properties

We initially folded BLPSR using the detection parameters obtained from `accelsearch`. To refine these parameters, we refolded the `filterbank` data using `prepfold`, and measured the DM that maximized the S/N (see Section 5.3). While a timing-based DM fit was attempted, it produced unrealistically small formal uncertainties. Instead, we adopted the DM and associated error estimated from the analysis in Section 5.3, which we consider more robust. Pulse TOAs were then derived from the `prepfold` file using the `pat` utility (part of the `PSRCHIVE` suite) employing Fourier-domain Monte Carlo techniques. The template profile for TOA generation was created by fitting a single Gaussian component to the full-average `prepfold` profile, using the `paas` routine in `PSRCHIVE`. Splitting the full 1 hr integration of Scan 1.1 into eight 7.5 minute subintegrations resulted in a median TOA uncertainty of ∼1 ms, or about 0.12 rotations. We then used `tempo2` with these TOAs to further refine the fundamental frequency and its first derivative during this observation. Figure 6 shows the BLPSR candidate folded using `prepfold` with this refined ephemeris. Although BLPSR is speculative, we summarize its final parameters in Table 3 to reference our discussion. We used the newly derived DM of 2775 pc cm^{-3} for the electron density models.[12] We noticed that after folding with the derived ephemeris, the folded profile exhibited a peak close to S/N ≈ 3. For additional verification, we dedispersed and folded the data using `dspsr` (W. van Straten & M. Bailes 2011) to generate a `PSRCHIVE`-formatted `archive` file (A. W. Hotan et al. 2004). We were able to see a similar, although relatively weaker, pulse profile (not shown here) in these data, confirming that the original detection shown in Figure 6 is not an artifact of our `PRESTO`-based pipeline.

[11] However, it should be noted that Gaussian noise can also produce peaks in the power spectrum, which, when incrementally summed over harmonics, may lead to an apparent increase in total coherent power at each step.

[12] Distance discrepancies between electron density models (NE2001 and YMW16) arise from different assumptions, including the distance of the GC from the Sun, the modeled Galactic components, and the use of interstellar scattering measurements (J. M. Cordes & T. J. W. Lazio 2003; J. M. Yao et al. 2017; D. C. Price et al. 2021).

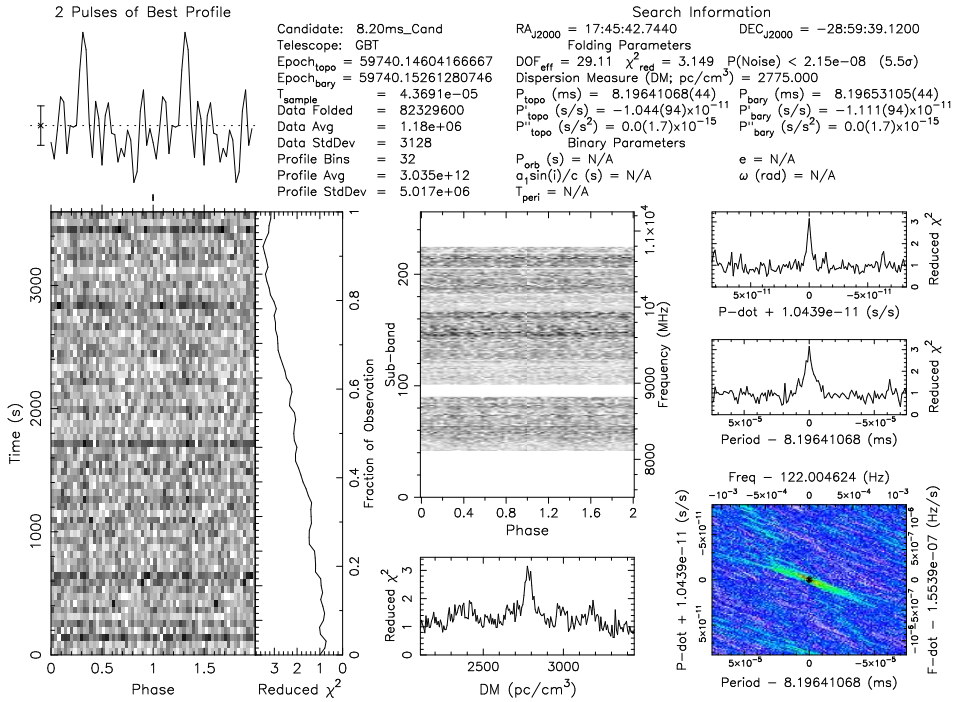

Figure 6. PRESTO (S. Ransom 2011) plot of the BLPSR candidate, folded using parameters from the .par file derived from time of arrival (TOA) measurements (see Section 5). Data were obtained with the GBT at a central frequency of $\nu_c = 9.37$ GHz on 2022 June 10, with a total integration time of 1 hr. The folded profile was generated using 32 phase bins and 256 subbands (each 14.65 MHz wide), with ∼1.2 GHz removed for signal clarity.

5.1. Data Quality Test

As noted in Section 4.3, BLPSR was only detected in the first 1 hr scan of Epoch 1 at a relatively low significance of the folded profile (around 3σ as seen in Figure 6). To verify this detection was not due to data quality issues, we attempted to find single pulses from the bright GC magnetar, SGR J1745–2900 (DM ≈ 1778 pc cm^{-3}), which is located well within our beam. This magnetar is known to regularly produce strong single pulses, which serves as an excellent benchmark for data quality. We used Heimdall (B. R. Barsdell et al. 2012) with our specialized machine learning candidate-sorting algorithm SPANDAK (V. Gajjar et al. 2022) to detect single pulses from all Epoch 1 scans (see V. Gajjar et al. 2021, for more details). Figure 8 shows the magnetar's single-pulse S/N as a function of MJD across the full five 1 hr scans in Epoch 1. It is consistently detected at a stable S/N level with no noticeable dropouts or systematic trends, indicating that our data quality remained consistent throughout the full epoch. A one-way analysis of variance across the five scans showed no statistically significant difference ($F = 0.3548$, p-value $= 0.84$) in the magnetar's mean S/N, including the first segment (Tukey's honestly significant difference test also confirmed this; p-value $= 0.97$). Hence, the nondetections (see Section 6.3 for further discussion) of BLPSR in scans beyond the first hour cannot be solely attributed to any sensitivity loss or other data quality issues.

5.2. Segmentation Test

A key test to validate a pulsar detection is to verify that the pulse profile persists across both time and frequency, as spurious interference or RFI seldom display such consistent behavior. Figure 9 shows the pulse profile divided into eight subintegrations and four frequency subbands. A relatively weaker, but statistically significant, integrated profile with $\sim 3\sigma$ significance can be seen. The profile remains visible in most subintegrations—except near the end of the observation—and is visible across most subbands, except at the lower frequencies. It is also evident that beyond ∼30 minutes in observing time, the per-subintegration S/N values drop to close to unity, indicating that the on-pulse bin is statistically indistinguishable from the off-pulse baseline; thus, the pulsar is not detected in the latter part of the observation. To quantify signal persistence, we performed a Kolmogorov–Smirnov (KS) test on each profile bin, comparing the on-pulse power distribution to the off-pulse distribution. For a real pulsar, we expect the power distribution for on-pulse bins to show significant deviations from the off-pulse bins (M. J. Keith et al. 2009). We refer to the measured KS statistics (and corresponding p-values) from subband comparisons across profile bins as the parameter for broadbandness and those from subintegration comparisons across profile bins as the parameter for time persistence as $D^{\rm KS}_{\rm broad}$ and $D^{\rm KS}_{\rm time}$, respectively (see Figure 9).

We found $D^{\rm KS}_{\rm broad} = 0.94$ (p-value $< 4 \times 10^{-4}$) for broadbandness across the full bandwidth and $D^{\rm KS}_{\rm time} = 0.62$ (p-value $< 2 \times 10^{-3}$) for time persistence across the full Scan 1.1, indicating that we can reject the null hypothesis that the on-pulse and off-pulse distributions are drawn from the same population. The relatively lower p-value associated with time persistency is likely due to BLPSR exhibiting an almost negligible profile roughly after the first 45 minutes (also seen in Figure 6); by ignoring the last 15 minutes, we found an expected improved p-value of $<2 \times 10^{-4}$. It should be noted, however, that although these probabilities and Figure 9 suggest the presence of a broadband signal persisting across a large fraction of the observing time—making spurious RFI unlikely—the observed S/N in each subband and subintegration is low enough that noise fluctuations could still mimic such behavior.

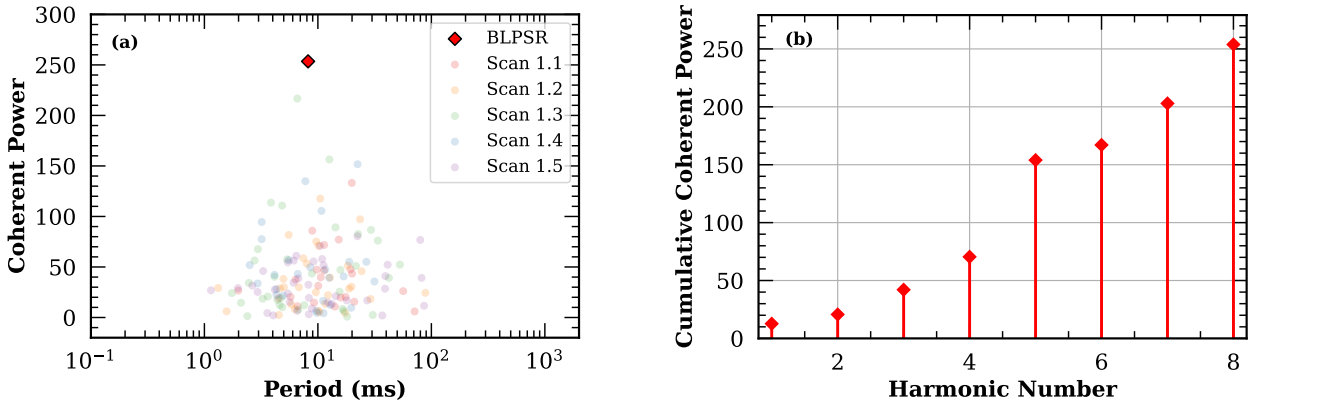

Figure 7. (a) Coherent power as a function of period (in milliseconds) for all candidates detected with $z_{\max} = 200$ during Epoch 1 using 4096 subbands. The BLPSR candidate, depicted by the red diamond, exhibits the highest coherent power among all detected candidates, strongly suggesting its astrophysical nature. (b) Cumulative coherent power as a function of harmonic number (n) for BLPSR. Each stem line represents the aggregated power up to $n = 8$, illustrating how the coherent power accumulates with each harmonic step as that expected for a real pulsar.

Table 3
Parameters of the Unconfirmed BLPSR Candidate

Parameter	Value
R.A. (J2000, hh mm ss.ss)[a]	17 45 40.04 ± 5.6
Decl. (J2000, dd mm ss.ss)[a]	−29 00 28.10 ± 1.4
$P_{s,0}$ (ms)	8.196531 (02)
$\dot{P}$ (s s^{-1})	$-1.111(12) \times 10^{-11}$
DM (pc cm^{-3})	2775 ± 24 (1σ)
$d_{\rm NE2001}$ (kpc)	8.59
$d_{\rm Y\ MW16}$ (kpc)	11.33
10 GHz min. flux density, $S_{\rm min,10\ GHz}$ (mJy)[b]	0.009
$L_{10\ \rm GHz} = S_{10\ \rm GHz}\ d^2$ (mJy kpc^2)	0.61
Pulse width at 10 GHz, W_{50} (ms)	<0.7

Notes.
[a] The position error corresponds to our 1⁄4 beamwidth.
[b] Assuming BLPSR was detected at the A00 pointing beam center.

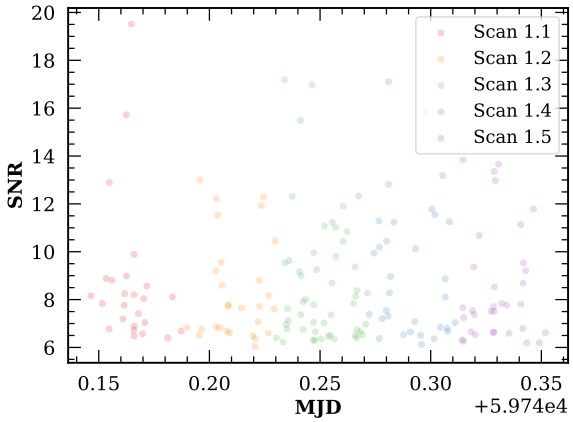

Figure 8. Single-pulse detections of the GC magnetar SGR J1745–2900 as a function of observation MJD. Each color corresponds to a different 1 hr scan from Epoch 1. The BLPSR candidate was only detected in the first scan, for which the magnetar single pulses are shown in red. The consistency of magnetar pulses across all scans indicates no apparent data quality issues during our observations.

Furthermore, the derived KS statistics are based on a small number of samples (four subbands and eight subintegrations across 16 profile bins). In other words, we cannot rule out the possibility that the detection is due to spurious noise or low-level RFI, and further tests were carried out in Section 5.4.

5.3. Peak Flux with Dispersion Measure

An important diagnostic for evaluating the astrophysical nature of BLPSR is a comparison of its folded profile peak amplitude S/N as a function of DM. Following J. M. Cordes & M. A. McLaughlin (2003), the reduction in S/N due to an incorrect DM (δDM) can be expressed by

$$\frac{S/N(\delta\mathrm{DM})}{S/N^{\max}} = \frac{\sqrt{\pi}}{2}\,\zeta^{-1}\,\mathrm{erf}(\zeta), \tag{7}$$

where

$$\zeta = 6.91 \times 10^{-3}\,(\delta\mathrm{DM})\,\frac{\Delta B}{W_{\rm ms}\,\nu_{\rm c}^3}. \tag{8}$$

Here, ΔB is the total bandwidth in megahertz, $\nu_{\rm c}$ is the center observing frequency in gigahertz, $W_{\rm ms}$ is the pulse width in milliseconds, and erf is the error function.

To test BLPSR, we began with the original `filterbank` file, dedispersed it at a DM of 2775 pc cm^{-3}, and used `prepfold` to fold the data into 4096 subbands with 64 profile bins each, using the ephemeris listed in Table 3. We then dedispersed the subbanded folded data (in `pfd` format) across a range of trial DMs, where, for each DM, a mean-subtracted folded profile was obtained. Visual inspection confirmed the expected profile broadening toward the trailing and leading edges when it was under- and overdispersed, respectively. To measure the peak S/N, each folded profile was multiplied with a top-hat (boxcar) function of varying width (S. Ransom 2011; B. R. Barsdell et al. 2012). We then visually inspected and selected the width that maximized the S/N within the on-pulse region. The off-pulse region was used to calculate the standard deviation and calculate the error in the measured S/N. We calculated these for each DM and normalized them by the maximum S/N$^{\max}$ across all DMs to compare the measured ratio with the ratio given in Equation (7).

The measured $\frac{\mathrm{S/N}(\delta\mathrm{DM})}{\mathrm{S/N}^{\max}}$ as a function of DM, along with their errors, are plotted in Figure 10. We then fitted these data with the expected distribution from Equation (7), treating both the pulse width and the DM offset as free parameters. The fitted model loosely matches the data with some degree of confidence ($\chi^2_{\rm reduced} \approx 0.23$; p-value $> 99\%$). The derived

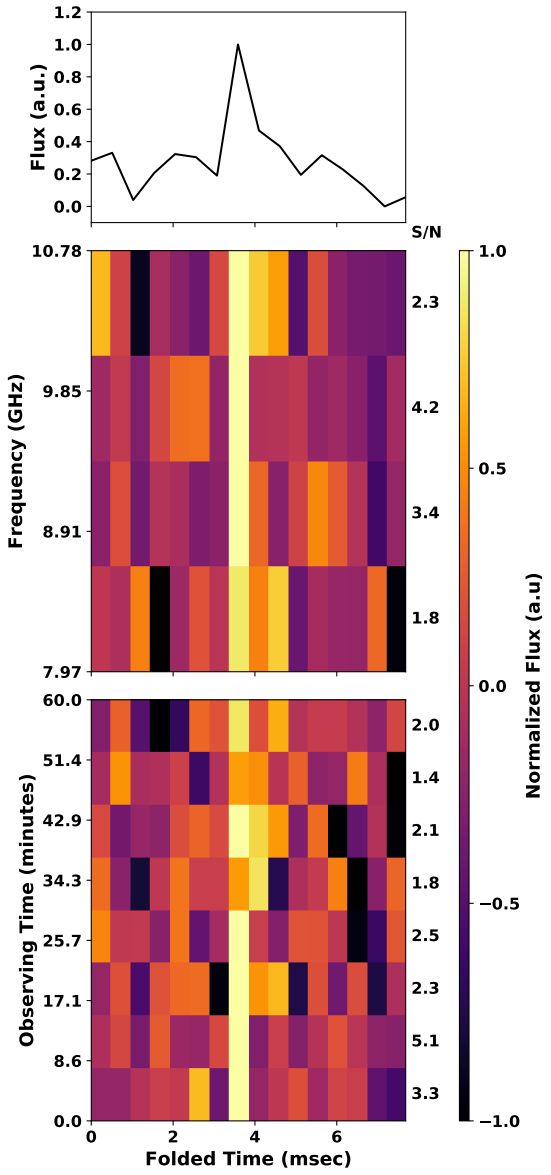

Figure 9. The folded profile of the candidate pulsar, BLPSR, detected from our survey is shown across four subbands and eight subintegrations, demonstrating consistent peaks across most segments. The corresponding peak S/N values are also shown separately for each subintegration and subband, highlighting the persistence of the signal across time and frequency. The overall average S/N of the folded profile is $\approx 3\sigma$, and the signal appears to gradually fade toward the end of the observation.

DM that provides the maximum S/N is 2775 ± 24 (1σ) pc cm^{-3}. Although the peak S/N follows the expected distribution, the relatively large error bars (as indicated by the low $\chi^2_{\rm reduced}$) imply that the variations in the peak S/N across DM are not statistically significant. As a result, we cannot conclusively determine that our candidate follows the expected distribution, so this test is inconclusive given the marginal quality of the detection.

5.4. Randomization Tests

Figure 9 offers a limited but suggestive indication that BLPSR could be a genuine astrophysical signal, and as discussed in Section 4.3, its detection properties warrant a deeper examination. However, BLPSR's relatively weak folded profile ($\chi^2_{\rm reduced} \sim 3$) and inconclusive peak S/N–DM

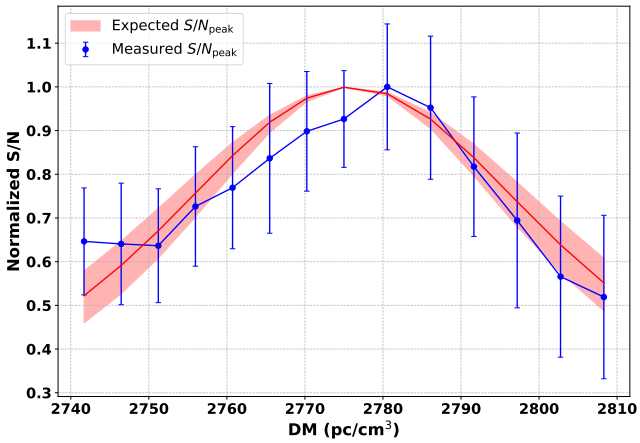

Figure 10. Measured peak S/N (blue) vs. DM for BLPSR, normalized to the highest measured S/N. The red curve is the best-fit model from J. M. Cordes & M. A. McLaughlin (2003), treating the pulse width as a free parameter. The pink shaded region indicates the range of theoretical S/N vs. DM curves spanned by the 1σ uncertainty in the fitted width.

variation (see Section 5.3) motivate a statistical probability estimate of two additional possibilities: that its detection could arise from very low-level RFI or random noise fluctuations within Scan 1.1.

To investigate this, we designed a novel randomization test to jointly evaluate the significance of BLPSR's observed properties. As a first step, and to reduce computational load, we downsampled the original `filterbank` data from 40,960 to 1024 frequency channels, preserving the 43.69 μs sampling time and omitting any dispersion correction. We also used `prepfold` to verify that BLPSR remained detectable with the previously derived ephemeris. With these scrunched data, we found $D^{\rm KS}_{\rm broad} = 0.96$ (p-value $< 4 \times 10^{-4}$) for broadbandness across the full bandwidth and $D^{\rm KS}_{\rm time} = 0.91$ (p-value $< 2 \times 10^{-6}$) for time persistence. The slight increase in KS statistics compared to the original data is expected since no frequency channels were flagged during the collapse. A blind $z_{\rm max} = 200$ search on this scrunched `filterbank` file again recovered BLPSR as the top candidate in both σ_{ps} and coherent power, out of 727 raw candidates. After applying the `sifting` algorithm to remove duplicates, only 36 unique candidates remained, all of which—except for BLPSR—were ultimately identified as spurious noise.

We then generated a fully randomized version of the aforementioned downsampled `filterbank` file by shuffling all time–frequency samples independently, thereby randomizing the entire dynamic spectrum while preserving the overall structure of 1024 frequency channels and 43.69 μs sampling time. This procedure destroyed any coherent, pulsarlike signal or low-level RFI, allowing us to assess the probability of recovering a BLPSR-like candidate from noise alone. We processed these randomized data through our standard pulsar search pipeline (see Figure 2) using the same parameters as in the original search. This yielded 533 raw candidates, which were subsequently reduced to 27 unique candidates after applying the `sifting` algorithm. However, because the data are entirely randomized, all candidates can be considered statistically independent noise realizations across all detected DMs and periods. Thus, to better characterize the noise distribution, we used all 533 raw candidates in the subsequent analysis.

Each candidate was folded using `prepfold` into 256 subbands, 64 subintegrations, and 16 profile bins, producing corresponding folded `pfd` files. These files were then collapsed into four subbands and eight subintegrations (similar to Figure 9) to evaluate their broadbandess and time-persistent KS statistics, $D^{\rm KS}_{\rm broad}$ and $D^{\rm KS}_{\rm time}$, respectively, as described in Section 5.2. While we did calculate p-values for each candidate, a more robust significance estimate comes from the randomization test described below, which benefits from a larger number of samples than the individual candidate KS-derived p-values.

We computed a joint probability distribution for BLPSR based on three independent parameters of this randomized candidate set: (i) the coherent power measured, and the KS-test statistics for (ii) $D^{\rm KS}_{\rm broad}$ and (iii) $D^{\rm KS}_{\rm time}$ of all 533 candidates. Although coherent power and $D^{\rm KS}_{\rm time}$ may appear correlated, they are not strictly dependent. Coherent power is computed from the sum of complex Fourier amplitudes, and can produce a significant peak with harmonics in the Fourier transform even if a strong periodic signal is present for only a brief portion of the observation. Thus, coherent power does not directly test for time persistence and can be treated as an independent property of BLPSR. Figure 11 shows the 3D distribution and correlation of these three critical parameters among the randomized candidates. To quantify the joint probability of our BLPSR candidate's parameters, we constructed a joint probability density using a Gaussian kernel density estimator (KDE), `scipy.stats.Gaussian_kde`. The KDE is given by

$$\hat{f}(\boldsymbol{x}) = \frac{1}{nh^d}\sum_{i=1}^{n} K\left(\frac{\boldsymbol{x}-\boldsymbol{x}_i}{h}\right), \tag{9}$$

$$K(\boldsymbol{z}) = \frac{1}{(2\pi)^{d/2}}\exp\left(-\frac{1}{2}\|\boldsymbol{z}\|^2\right), \tag{10}$$

where n is the number of candidate samples, d is the number of parameters, and h is the smoothing bandwidth. We follow Scott's normal-reference rule (D. W. Scott 1992), which gives the asymptotic mean integrated squared error optimal bandwidth for a d-variate KDE with a Gaussian kernel: $h_j = c_d\,\hat{\sigma}_j\,n^{-1/(d+4)}$, where $\hat{\sigma}_j$ is the sample standard deviation of parameter j and $c_d = (4/(d+2))^{1/(d+4)}$. In our implementation using `scipy.stats.Gaussian_kde`, this scalar bandwidth factor $n^{-1/(d+4)}$ is applied in combination with the full sample covariance matrix of the parameters, which automatically accounts for differences in scale and correlations between dimensions (see P. Virtanen et al. 2020). This approach ensures that the KDE reflects the underlying data density. The resulting KDE thus provides a continuous, smooth estimate of the probability density function in the joint parameter space spanned by coherent power, $D^{\rm KS}_{\rm broad}$, and $D^{\rm KS}_{\rm time}$.

As is evident from Figure 11, BLPSR lies at the extreme tail of all three parameter distributions. To thoroughly explore the tail of this multidimensional distribution, we implemented a simple random-walk Markov Chain Monte Carlo (MCMC) sampler based on the Metropolis–Hastings algorithm. Starting from the BLPSR candidate's parameter vector, $\boldsymbol{x}_{\rm det}$, the MCMC sampler generated 10^8 samples, $\{\boldsymbol{x}_j\}_{j=1}^{N_{\rm MCMC}}$, from the KDE. For each sample, the KDE density $\hat{f}(\boldsymbol{x}_j)$ was computed, and the joint p-value was then estimated as

$$P_{\rm joint} = \frac{1}{N_{\rm MCMC}}\sum_{j=1}^{N_{\rm MCMC}} \mathbf{1}(\hat{f}(\boldsymbol{x}_j) \leqslant \hat{f}(\boldsymbol{x}_{\rm det})), \tag{11}$$

where $\mathbf{1}(\cdot)$ denotes the indicator function, which returns one if the condition is satisfied and zero otherwise. In this case, it counts the fraction of MCMC samples whose estimated KDE density is less than or equal to that of BLPSR $\boldsymbol{x}_{\rm det}$, thereby providing a quantifiable estimate of the joint tail probability of observing a candidate as rare or rarer than BLPSR among the noise-generated candidates.

This MCMC-based resampling method allowed for a high-resolution estimation of the tail probability within the joint parameter space of coherent power, $D^{\rm KS}_{\rm broad}$, and $D^{\rm KS}_{\rm time}$. We find a resulting joint p-value of $P_{\rm joint} < 5\times10^{-7}$, indicating that BLPSR's overall properties are extremely rare in the multi-dimensional space. By comparison, a joint p-value computed using only the KS statistics yielded a less significant $P_{\rm joint} < 8\times10^{-3}$. This outcome is expected at the very low folded profile significance of BLPSR, $\sim3\sigma$, which gives rise to weaker subband and subintegration profiles. For completeness, we also applied the same analysis to the 727 raw candidates detected in the original downsampled 1024 channel frequency-scrunched `filterbank` file. These candidates showed similarly extremely low $P_{\rm joint}$ probabilities; however, because the raw candidates are not completely independent as stated earlier, we do not consider them for our statistical interpretation.

From this randomization test, there remains approximately a one-in-a-million probability of finding a BLPSR-like candidate with similar properties purely from noise. It should be noted that, in order to maximize the number of candidates in our analysis, no sifting was applied during the randomization test. However, had we restricted the analysis to only candidates that did pass our duplicate rejection criteria—as BLPSR did—the likelihood of finding such a candidate from noise alone would be even lower. While these odds are noteworthy, they must be interpreted within the broader context of the large number of trials performed across five dimensions—DM, f, $N_{\rm H}$, $z_{\rm max}$, and $w_{\rm max}$—as mentioned in Section 3. In other words, although BLPSR may indeed be a real pulsar, current evidence remains insufficient to support that claim with high statistical significance.

6. Discussion

6.1. Known Galactic Center Region Pulsars

Currently, six pulsars—excluding the GC magnetar—are known within 1° of Sgr A*. Of these, three (PSR J1746–2850I, PSR J1746–2850II, and PSR J1745–2910) lie within 12′ (∼30 pc in projection) of the SMBH (J. S. Deneva et al. 2009). Three additional pulsars are located within 18′ (∼40 pc in projection): PSR J1745–2912 and PSR J1746–2856 (S. Johnston et al. 2006) and PSR J1744–2946 (M. E. Lower et al. 2024). The latter is the fastest ($P = 8.4$ ms) MSP detected near the GC to date. However, its low DM (∼674 pc cm^{-3}) implies that it resides in the foreground along the line of sight and is not physically close to the GC. While these discoveries support the presence of a large pulsar population near the GC, none lie close enough (within a parsec) to the SMBH to probe its gravitational field (K. Liu et al. 2012). Furthermore, all known

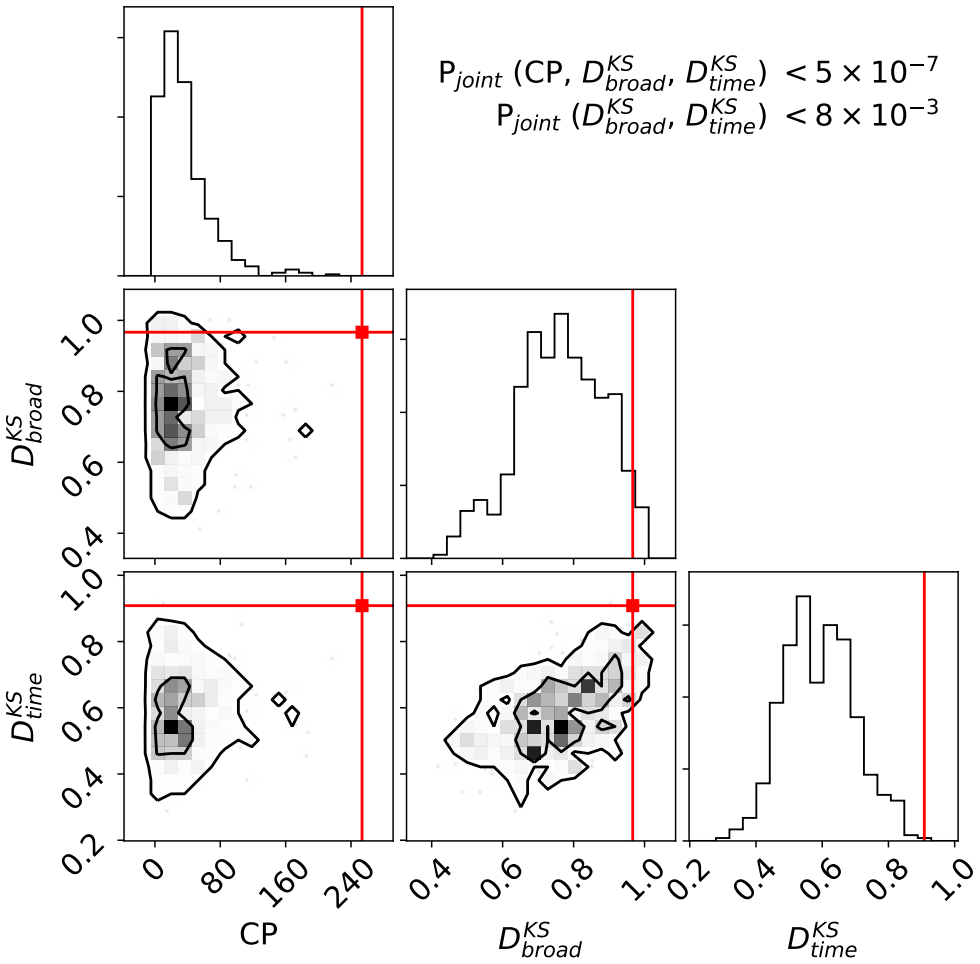

Figure 11. Corner plot showing the joint distribution of coherent power, broadband KS statistic ($D^{\rm KS}_{\rm broad}$), and time-persistent KS statistic ($D^{\rm KS}_{\rm time}$) for candidates from the randomized `filterbank` search. Contour lines enclose 50% and 99% of the total probability density under the KDE. Red lines mark the BLPSR candidate values, which lie at the tail end of all three distributions. The computed joint probability of BLPSR under the 3D KDE model is $P_{\rm joint} < 5 \times 10^{-7}$, indicating a highly significant deviation from noise (primarily due to its high coherent power). For comparison, the joint p-value using only the two KS statistics is less significant at $P_{\rm joint} < 8 \times 10^{-3}$.

pulsars in the region fall outside the primary beam of our survey and were therefore not detected in our observations. In the following subsection, we detail our sensitivity limits and compare them to other previous surveys conducted toward the GC.

6.2. Highest Sensitivity to Galactic Center Pulsars

We estimated our survey's pulsar detection sensitivity using 2167 known field pulsars from the Australian National Telescope Facility (ATNF) catalog 2.6.3 (R. N. Manchester et al. 2005).[13] We derived their 1.4 GHz luminosity using $S \times d^2$, where S and d are the catalog parameters `S1400` and `DIST_A`, respectively, corresponding to the mean flux density at 1.4 GHz (in millijanskies) and the distance based on an dependent distance estimate. `DIST_DM`, the distance based on the YMW16 electron density model, was used where `DIST_A` was not available. Additional 2176 pulsars were excluded from this analysis due to missing relevant parameter values. To compare these with our X-band observations at $\nu_c \approx 10$ GHz, we scaled their luminosities using $L_{1.4} = L_{\nu_c}(1.4/\nu_c)^{\alpha}$, where α is the spectral index. We adopt $\alpha = -1.76$ for CPs and $\alpha = -1.95$ for MSPs, where MSPs are defined as those with $P < 30$ ms (P. Torne et al. 2021). The black points in Figure 12 show the distribution of these known pulsars in period–pseudoluminosity space.

We now define $L_{\nu_c} = S_{\rm min}\, d^2_{\rm GC}$, where $S_{\rm min}$ represents the minimum detectable flux density, and $d_{\rm GC}$ is the distance to the GC (8.18 kpc; R. Abuter et al. 2019). $S_{\rm min}$ can be expressed by the radiometer equation (D. R. Lorimer & M. Kramer 2004)

$$S_{\rm min} = \frac{\mathrm{S/N_{min}}\, T^{\rm GC}_{\rm sys}}{G\,\sqrt{n_p\, t_{\rm int}\, \Delta\nu}}\,\sqrt{\frac{\delta}{1-\delta}}, \tag{12}$$

where $T^{\rm GC}_{\rm sys}$ is the net system temperature toward the GC (K. O'Neil 2002; A. Suresh et al. 2021). $T^{\rm GC}_{\rm sys}$ is defined by

$$T^{\rm GC}_{\rm sys}(\nu_c, t) = T_{R_g}(\nu_c) + (T_{\rm GC}(\nu_c) + T_{\rm CMB})\, e^{-A(t)\,\tau_{\nu_c}} + T_{\rm atm}\,(1 - e^{-A(t)\,\tau_{\nu_c}}), \tag{13}$$

where $T_{\rm GC}(\nu_c) \approx 568\ \mathrm{K}\ (\nu_c/1\ \mathrm{GHz})^{-1.13}$ is the background continuum temperature in the direction of the GC (K. M. Rajwade et al. 2017; V. Gajjar et al. 2021). $T_{\rm CMB} \approx 2.73$ K is the isotropic cosmic microwave background (CMB) temperature

[13] https://www.atnf.csiro.au/research/pulsar/psrcat/

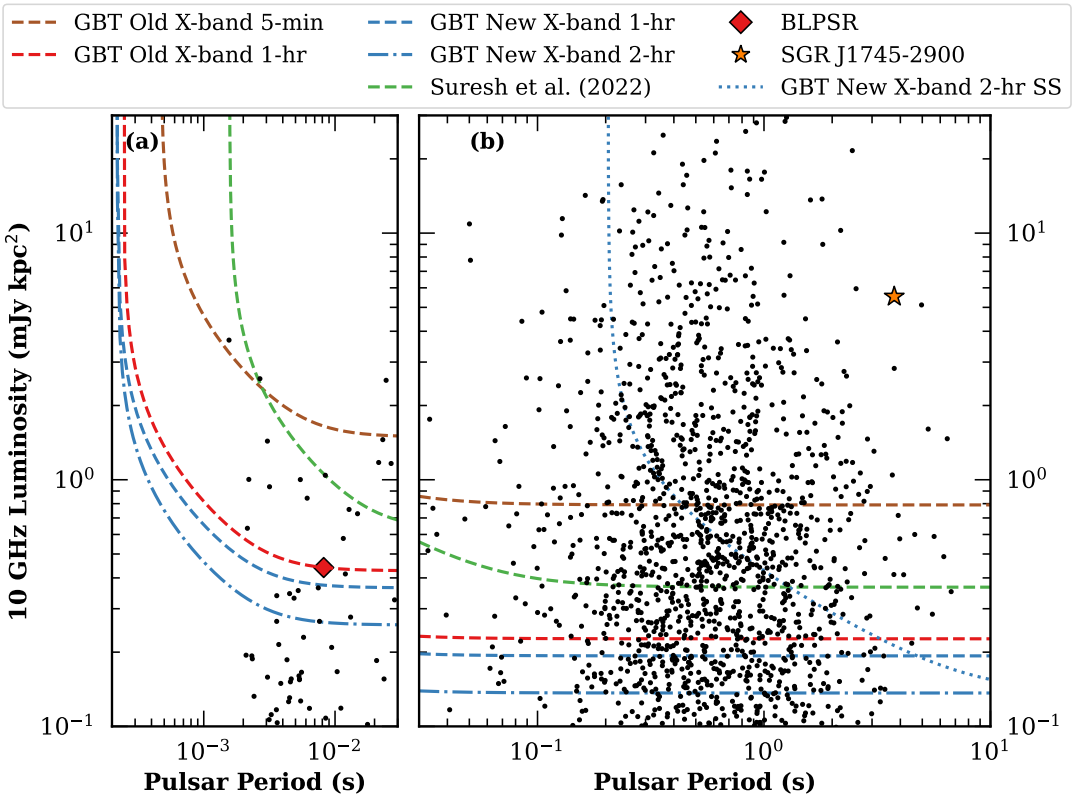

Figure 12. GBT 3σ sensitivity curves at *X*-band for our 5 minute, 1 hr, and 2 hr integrations. Black dots indicate known field pulsars from the ATNF catalog, plotted in period–pseudoluminosity space. Their flux densities have been scaled to 10 GHz assuming a power-law spectrum with spectral indices of $\alpha = -1.76$ for CPs and $\alpha = -1.95$ for MSPs. The figure is split into two panels at $P_0 = 30$ ms to separate (a) MSPs ($P_0 < 30$ ms) and (b) CPs ($P_0 > 30$ ms), with different duty cycles and spectral indices used for each. The brown dashed line corresponds to the 5 minute integrations used for all 37 short pointings. The red dashed line represents the 1 hr integration used for Epoch 1 with the old *X*-band receiver (7.50–11.25 GHz). The blue dashed–dotted line denotes the 2 hr integration used for Epoch 2, and the blue dashed line shows their 1 hr segments with the new *X*-band receiver (7.50–12.38 GHz). For comparison, the green dashed line shows the predecessor BL-GC survey at *C* band (4–8 GHz) conducted with the GBT (A. Suresh et al. 2022). All curves assume weak scattering toward the GC. However, under strong-scattering conditions, even our most sensitive observation (Epoch 2; 2 hr integrations) would only detect pulsars with $P_0 \gtrsim 0.2$ s (dotted blue line). The orange star denotes the lowest flux density recorded for the GC magnetar J1745–2900, although it has been observed to fluctuate over the years, detected as high as ∼440 mJy (R. P. Eatough et al. 2013b; Z. Yan et al. 2015; A. B. Pearlman et al. 2018; A. Suresh et al. 2022). The red diamond shows our BLPSR candidate. We note that we chose a cutoff of 0.1 mJy kpc^2 for our $L_{\rm min}$(10 GHz) axis to zoom into our sensitivity curves.

(D. J. Fixsen 2009), and $T_{\rm atm} \approx 269$ K is the estimated atmospheric temperature at $\nu_c = 10$ GHz.[14] The contribution of the atmosphere to $T_{\rm sys}^{\rm GC}$ at $\nu_c = 10$ GHz at our observed elevations is significantly lower, as it is modulated by the opacity term $1 - e^{-A(t)\,\tau_{\nu_c}}$. $\tau_{\nu_c} \approx 10^{-4}\left(80 + 1.25\,e^{\sqrt{\frac{\nu_c}{1\,\rm GHz}}}\right)$ represents the zenith atmospheric opacity[15] and $A(t) = 1/\sin(\theta_{\rm GC}(t))$ measures the airmass at the elevation $\theta_{\rm GC}(t)$ of the GC. For brevity, we take the mean $\theta_{\rm GC}(t)$ for all observations at each epoch and find $\theta_{\rm GC}(t) = 19.^\circ7$and $18.^\circ7$, for Epoch 1 and 2, respectively. Using these elevation angles and a zenith opacity of $\tau_{\nu_c} \approx 0.011$ at 10 GHz, we compute atmospheric attenuation factors of $e^{-A(t)\,\tau_{\nu_c}} \approx 0.968$ and 0.966 for Epoch 1 and 2, respectively. $T_{R_g}(\nu_c)$ denotes the receiver temperature of 17 K for $\nu_c = 10$ GHz (see the GBT Proposer's Guide).[16] We calculate a $T_{\rm sys}^{\rm GC}$ of 72 and 70 K for Epoch 1 and 2, respectively. The GC and CMB terms are modulated by the frequency- and elevation-dependent atmospheric opacity (e.g., GBT Memos #16, #19, and #302). Rear spillover contributes negligibly to the overall $T_{\rm GC}(\nu_c)$ at $\nu_c = 10$ GHz for the GBT due to its offset Gregorian design and low spillover efficiency ($\eta_l = 0.99$, see GBTIDL Calibration Guide and footnote 15), and is not included in Equation (13).

We use $\rm S/N_{min} = 3$, $G = 2$ K J^{-1} for the telescope gain, and $n_p = 2$ for the number of polarizations. $t_{\rm int}$ is the integration time and $\Delta\nu$ is the frequency bandwidth, which varies for the observations (see Section 2.2 for details). $\delta = W_{\rm eff}/P$ is the pulsar duty cycle, which is estimated using the ratio W_{50}/P, where W_{50} is the FWHM obtained from the ATNF catalog. This yields median duty cycles of 2.58% for CPs and 8.63% for MSPs. The effective pulse width takes into account the effects of scattering, dispersion, and instrumentation, and is given by

$$W_{\rm eff} = \sqrt{W_{\rm int}^2 + \tau_s^2 + \Delta t_{\rm DM}^2 + \delta t^2}, \quad (14)$$

where $W_{\rm int} = \delta P$ is the intrinsic pulse width, τ_s is the scattering timescale, $\Delta t_{\rm DM}$ is the intrachannel dispersion smearing (N. Clarke et al. 2013), and δt is the time resolution of the digitized data (R. N. Manchester et al. 1996).

We consider the weak-scattering model, as observed for PSR J1745–2900 (L. G. Spitler et al. 2014), $\tau_{ws} = 1.3\nu_{\rm GHz}^{-4}$ s. Although earlier studies such as J.-P. Macquart & N. Kanekar (2015) have explored the strong-scattering regime using a

[14] http://www.greenbankobservatory.org/~rmaddale/WeatherGFS3/tatm.html
[15] https://www.gb.nrao.edu/GBT/DA/gbtidl/gbtidl_calibration.pdf
[16] http://www.gb.nrao.edu/scienceDocs/GBTog.pdf

Table 4
Comparison of this Survey with Previous Deep Pulsar Searches of the Galactic Center

Survey	Telescope	ν_c (GHz)	$\Delta\nu$ (GHz)	$t_{\rm int}$ (hr)	$L_{\rm min}(\nu_c)$[a] (mJy kpc^2)	$L_{\rm min}$(10 GHz)[a,b] (mJy kpc^2)	No. detected
S. Johnston et al. (2006)	Parkes	3.1	0.576	1.2	66.9	≈7	2
S. Johnston et al. (2006)	Parkes	8.4	0.864	1.2	13.4	≈10	0
J. S. Deneva et al. (2009)	GBT	1.95	0.600	1	434.9	≈18	3
J.-P. Macquart et al. (2010)	GBT	14.6	0.800	<10[c]	40	≈84	0
R. P. Eatough et al. (2021)	Effelsberg	8.35	0.5	2.4[d]	4.68	≈3	0
R. P. Eatough et al. (2021)	Effelsberg	18.95	2	2.4[d]	3.35	≈12	0
K. Liu et al. (2021)	ALMA	86.3	2	5.2[e]	2.01	≈134	0
P. Torne et al. (2021)	IRAM 30 m	120	32	2.2[f]	3.95	≈502	0
A. Suresh et al. (2022)[g]	GBT	6.1	3.0	0.5	2.51	≈1	0
This survey:							
Short pointings	GBT	9.37	3.69	0.0833	1.60	1.60	0
Long pointings Epoch 1	GBT	9.37	3.75	1	0.44	0.44	1 candidate
Long pointings Epoch 2	GBT	9.94	3.75	1	0.37	0.37	0
Long pointings Epoch 2	GBT	9.94	4.88	2	0.26	0.26	0

Notes.
[a] Using $d_{\rm GC} = 8.18$ kpc (R. Abuter et al. 2019).
[b] $L_{\rm min} \propto \nu^{\alpha}$ is invoked, where $\alpha = -1.95$ is the mean spectral index of MSPs (P. Torne et al. 2021). These estimates do not account for scattering differences at 10 GHz.
[c] Maximum integration of a combined scan was 10 hr.
[d] Maximum scan duration (R. P. Eatough et al. 2021).
[e] Composed of individual scans of ≈3–6 minutes each that were coherently connected.
[f] Mean $t_{\rm int}$ calculated from the 28 observations in P. Torne et al. (2021).
[g] Recalculated luminosity from that derived in A. Suresh et al. (2021). We apply our median values of α and δ for MSPs and CPs for greater consistency in comparing it to this survey, and use their $S/N_{\rm min} = 6$.

scattering screen located ≈130 pc from the GC, they estimate that the optimal search frequency for detecting MSPs under such conditions is ≈25 GHz, which is beyond the range of our survey.

The intrachannel smearing is calculated by

$$\Delta t_{\rm DM} = \frac{2\ DM\ \Delta\nu_{\rm subband}}{\kappa\ \nu_c^3}, \quad (15)$$

where $\Delta\nu_{\rm subband}$ is the subband bandwidth, $\kappa = 2.41 \times 10^{-16}$ pc cm^{-3} s, and DM = 1778 pc cm^{-3} (for PSR J1745–2900) is chosen. Because smearing within each of the 4096 subbands is negligible (see Section 2.3), we are sensitive to the fastest MSPs and their harmonics.

Our sensitivity measurements align with pulsar detection estimates toward the GC, demonstrating that our survey is capable of detecting the brightest MSPs under the assumption of weak scattering (Figure 12), provided that the intrinsic GC pulsar population is comparable to that of the broader Milky Way. Our long pointings achieved the highest sensitivity of any GC survey to date, and the lower half of Table 4 summarizes the corresponding $S_{\rm min}$ and $L_{\rm min}$ values for MSPs (assuming $P_0 \approx 10$ ms), which are the primary focus of this survey. For the BLPSR candidate, we assume the median MSP duty cycle for consistency ($\delta = 8.63\%$), where its ≈3σ detection corresponds to a flux density of $S_{10\ \rm GHz} \approx 0.007$ mJy and a radio luminosity of $L_{10\ \rm GHz} \approx 0.44$ mJy kpc^2. For our survey threshold of $S/N_{\rm min} = 3$, we obtain corresponding $S_{\rm min}$ values of 0.02 mJy (short pointings), 0.007 mJy and 0.006 mJy (1 hr long pointings for Epochs 1 and 2, respectively), and 0.004 mJy (2 hr long pointings) for MSPs. Figure 12 also shows our sensitivity for CPs (>30 ms), with the full 2 hr Epoch 2 integrations reaching $S_{\rm min} \approx 0.002$ mJy and $L_{\rm min} \approx 0.14$ mJy kpc^2(assuming $P_0 \approx 1$ s). In contrast, even our most sensitive observation (Epoch 2; 2 hr integrations) would only be sensitive to pulsars with $P_0 \gtrsim 0.2$ s under strong-scattering conditions (dotted blue line).

Several other deep pulsar searches have also targeted the GC using various radio telescopes—including Effelsberg, the GBT, and Parkes—covering frequencies up to 156 GHz (P. Torne et al. 2021). Table 4 summarizes the key parameters of these prior surveys (top half). For cross-survey sensitivity comparison, we report their minimum detectable luminosities, $L_{\rm min}(\nu_c)$, using $d_{\rm GC} = 8.18$ kpc, and we also scale them to $\nu_c = 10$ GHz ($L_{\rm min}$(10 GHz)), assuming a power-law spectral index of $\alpha = -1.95$ for MSPs (P. Torne et al. 2021). We do not include the $S/N_{\rm min}$ or $S_{\rm min}$ from previous surveys, as these are based on different detection criteria, making direct comparison inconsistent. As seen in Table 4, out of all previous surveys, the Parkes survey at $\nu_c = 8.4$ GHz with a 1.2 hr integration time (S. Johnston et al. 2006) is the most similar to our *X*-band observations but suffers from a reduced bandwidth and smaller effective area, which limit its sensitivity to MSPs unless their luminosity exceeds 13.4 mJy kpc^2. The final column lists the number of pulsars (or candidates) detected by each survey, most of which are outlined in Section 6.1.

Figure 12 also shows the sensitivity curve for the previous BL-GC survey at *C* band (4–8 GHz) conducted with the GBT (A. Suresh et al. 2022). While an $L_{\rm min}$(10 GHz) of ≈1 mJy kpc^2 was achieved for MSPs, the shorter integration time of 30 minutes and lower frequency coverage in A. Suresh et al. (2022) likely compromised any detections due to the complex pulsar orbital dynamics and scattering effects expected in the GC. Additionally, the coverage in the 1.4–6 GHz range likely also impeded the detection of MSPs due to their inherent

faintness (K. M. Rajwade et al. 2017) and extended eclipses in binaries at low frequencies (see Section 6.5). Our BL-GC *X*-band survey with the GBT represents one of the most sensitive pulsar searches ever conducted toward the GC.

6.3. BLPSR Follow-up

BLPSR was detected only in Scan 1.1 of Epoch 1 during our blind searches. Following its initial detection, we conducted targeted follow-up searches on the subsequent four 1 hr scans of Epoch 1. These searches employed `prepfold` with 512 subbands, the corresponding `mask` file, and the ephemeris derived in Section 5, utilizing both the `-coarse` and `-fine` flags. We searched both with and without (`-nosearch`) constraints in P–$\dot{P}$ and DM–ϕ space, allowing for up to ± 4 full pulse phase wraps of error to accommodate the expected pulse phase drift over the duration of each observation. The parameter space spanned a spin frequency range of $f_s \pm 0.00\overline{1}$ Hz with a step size of $4.34027\overline{7} \times 10^{-6}$ Hz, and a spin frequency derivative range of $\dot{f}_s \pm 3.086 \times 10^{-7}$ Hz s^{-1} with a step size of 2.411×10^{-9} Hz s^{-1}—searching over 513 different trial values for f_s and $\dot{f}_s$. The `-coarse` flag examined 385 DMs (step size of 3.47 pc cm^{-3}), while the `-fine` flag covered 129 DMs (step size of 1.74 pc cm^{-3}), constituting an extensive parameter search. We also blindly searched Scans 1.1 and 1.2 coherently but did not recover the signal, likely because the BLPSR had already begun fading during the latter half of Scan 1.1 (see Section 5.2).

We applied the same targeted searches described above to the 2 hr scans from Epoch 2 and further subdivided them into 1 hr segments to accommodate possible variations in pulsar acceleration due to binary motion. This expanded our search parameter space, improving sensitivity to a wider range of orbital periods and accelerations (see Figure 3), since some pulsars can be eclipsed or exhibit varying acceleration over portions of their orbit (see Section 6.5 for more details). Despite these thorough targeted searches, BLPSR was not redetected.

6.4. Is BLPSR a Real Pulsar?

We have presented and discussed the observed properties of our BLPSR candidate and conducted a series of extensive tests to evaluate its significance, along with detailed follow-up observations, all of which resulted in nondetections. To summarize, BLPSR was identified as a top candidate in our acceleration search, exhibiting the highest coherent power and Gaussian significance (see Sections 4.2 and 4.3). It displayed pulsarlike properties across both time and frequency, and showed a relatively weak but noticeable peak in the S/N–DM plane (Figure 6). However, it was not detected in any subsequent observations (see Section 6.3).

In Section 5.1, we examined the quality of the immediate follow-up data (Scans 1.2–1.5) and found no evidence of sensitivity loss or instrumental issues that could plausibly explain the nondetection. In Section 5.3, we attempted to verify the expected variation of the peak S/N with DM but were unable to draw a robust conclusion due to the low signal strength. When visualizing the candidate across both time and frequency, and measuring the KS statistics for broadbandness and time persistency ($D^{\rm KS}_{\rm broad}$ and $D^{\rm KS}_{\rm time}$, respectively), we found evidence of significant structure, as would be expected for a true pulsar.

To evaluate whether such features could arise from noise alone, we carried out a novel randomization test (Section 5.4). When considering only the KS statistics, we found that roughly one in a 1000 noise-originating candidates could exhibit similar values, which is likely due to a lower-S/N folded profile. However, when factoring in BLPSR's unusually high coherent power, the likelihood of a noise fluctuation producing such a candidate dropped to approximately one in a million. Despite these results, we refrain from concluding that BLPSR is a real pulsar due to several key limitations. Its folded profile, while coherent, was relatively narrow and close to our detection threshold. More importantly, BLPSR was not redetected in either the immediate follow-up scans or in subsequent observations conducted nearly a year later using a different, more sensitive receiver (see Section 6.3).

In light of these factors—and given the extraordinary implications of detecting a pulsar near Sgr A*—we remain highly skeptical of BLPSR and emphasize that a much stronger burden of proof is required before asserting its astrophysical origin. Nonetheless, in the following subsections, we explore the possible orbital constraints and astrophysical scenarios that could explain its nondetection in subsequent follow-up observations. In summary, we remain dubious of the astrophysical nature of BLPSR, but recognize the possibility that it may be a real, yet highly variable or intermittent pulsar—potentially influenced by extreme propagation effects, binary motion, or intrinsic emission variability. Given its anomalous nature, BLPSR merits continued scrutiny and targeted reobservation efforts, though we withhold any definitive classification pending further evidence.

6.5. BLPSR Orbital Constraints and Astrophysical Scenarios for Nondetections

In Section 5.4, we explored the possibility that BLPSR may have arisen from noise fluctuations, which could explain its singular detection and absence in subsequent scans and epochs. The signal also appears to diminish in significance toward the end of the corresponding scan, prompting us to consider several astrophysical factors that could complicate redetection, particularly for a pulsar in a binary system near the GC, such as complex orbital dynamics and interactions within the dense stellar environment. The strong variability in scattering screen properties and the poorly understood high-electron-density environment in the GC is caused by fluctuations in the interstellar medium (T. J. W. Lazio & J. M. Cordes 1998; J. Dexter et al. 2017; F. Abbate et al. 2023). These variations are dependent on the pulsar's orbital position, as well as the uniformity (uniform versus patchy), movement rate, and distance of the intervening scattering screen (T. J. W. Lazio & J. M. Cordes 1998; J. Dexter et al. 2017). Such complex propagation effects could cause normally persistent pulsed signals into being highly intermittent, further complicating pulsar detection efforts near the GC. If BLPSR is indeed a genuine astrophysical signal, these factors could naturally lead to intermittent visibility or short-term detectability windows, complicating confirmation efforts from our follow-up observations.

Even our single detection of the candidate pulsar BLPSR constrains its orbital parameters significantly. The candidate was blindly detected at $z = 2.75$, corresponding to line-of-sight acceleration $a_l = -0.45\,\mathrm{m\,s^{-2}}$ during Scan 1.1, as noted in Section 4.3. This tentative nonzero acceleration may indicate

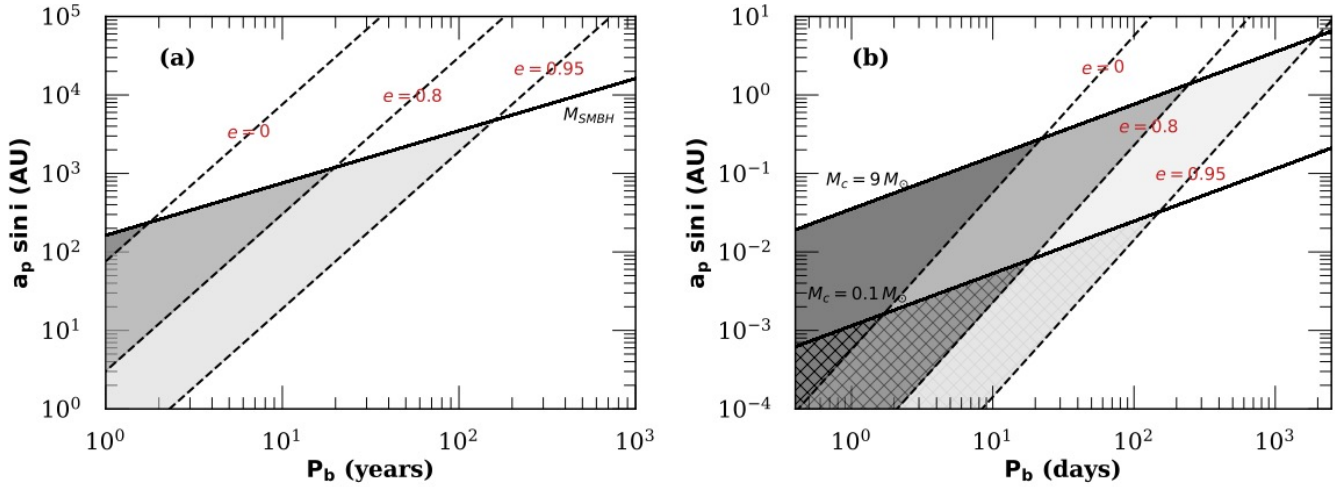

Figure 13. Allowed parameter space for the orbital period P_b and projected semimajor axis $a_p \sin i$ of BLPSR, assuming it is orbiting (a) the SMBH Sgr A* ($M_{\mathrm{Sgr\,A*}} = 4.30 \times 10^6\,M_\odot$), or (b) a stellar-mass companion of either $M_c = 9\,M_\odot$ or $M_c = 0.1\,M_\odot$. The solid black lines represent Kepler's third law for the true semimajor axis a_p, which is the upper limit on $a_p \sin i$, while the dashed lines are the lower limits on $a_p \sin i$ for different orbital eccentricities ($e = 0$, 0.8, and 0.95). The shaded regions, bounded by solid and dashed lines, mark the allowed parameter space for each eccentricity, including the full ranges of A_T and ω. The intersection point of a solid and dashed line marks the overall maximum P_b and a_p permitted for each eccentricity. In (b) the cross-hatched region represents the allowed parameter space for $M_c = 0.1\,M_\odot$, which is nested within that of $M_c = 9\,M_\odot$.

that it is in a binary system. We employ Equation (1) for a_l as a function of orbital parameters (M. Bagchi et al. 2013; K. Liu et al. 2021), which determines the ranges of a_p and P_b that could produce the observed $a_l = -0.45\,\mathrm{m\,s^{-2}}$ at some point along the orbit. For a given value of e, the angles that maximize the right side of Equation (1) are $A_T = 0$, and $\omega = \pi/2$. By choosing these angles, Equation (1) yields the minimum possible value of the projected semimajor axis $a_p \sin i$ as a function of P_b for a particular e, illustrated by the dashed lines in Figure 13. Then, for a particular assumed mass, a_p as a function of P_b is given by Kepler's third law, which represents the maximum possible value of $a_p \sin i$ (solid line in Figure 13). Finally, the intersection point of the solid and dashed line marks the overall maximum of P_b and a_p for the chosen M and e.

We explore these orbital constraints for a pulsar mass of 2.14 $M_\odot$, three different companion masses, and eccentricities $e = 0$, 0.8, and 0.95. First, we consider the SMBH Sgr A* ($M_{\mathrm{Sgr\,A*}} = 4.30 \times 10^6\,M_\odot$) as the companion. Figure 13(a) defines the allowed ranges of $a_p \sin i$ and P_b, which for each eccentricity form the shaded region between the corresponding dashed line and the solid line. At $e = 0$, the apex of the darkest shaded triangle indicates the maximum $a_p = 237.89$ au, corresponding to $P_b = 1.77$ yr. For $e = 0.85$, the maximum $a_p = 1189.78$ au at $P_b = 19.80$ yr, while for $e = 0.95$, the maximum $a_p = 4759.22$ au at $P_b = 158.39$ yr.

Similarly, Figure 13(b) presents the same eccentricity cases, but for a stellar-mass BH companion ($M_c = 9\,M_\odot$) and a representative redback or white dwarf companion ($M_c = 0.1\,M_\odot$). Given the significantly lower companion masses compared to Sgr A*, the corresponding orbital periods P_b are much shorter—on the order of days. For the stellar-mass BH ($M_c = 9\,M_\odot$), the maximum orbital period for $e = 0$ is 22.0 days, which corresponds to $a_p = 0.28$ au. For $e = 0.8$, the maximum P_b increases to 247.22 days with $a_p = 1.39$ au, while for $e = 0.95$, it extends to 1978.0 days with $a_p = 5.56$ au. The allowed parameter space for $M_c = 0.1\,M_\odot$ is nested within that of $M_c = 9\,M_\odot$, but with different maximum values, as indicated by the cross-hatched regions. For $M_c = 0.1\,M_\odot$, the maximum P_b for $e = 0$ is 1.6 days, which corresponds to $a_p = 0.0016$ au. For $e = 0.85$, the maximum P_b is 18.80 days with $a_p = 0.008$ au, and for $e = 0.95$, P_b reaches 147.61 days with $a_p = 0.03$ au.

Redback binaries are known to produce broad eclipses throughout their orbit, particularly around superior conjunction, when the companion star is between us and the pulsar. Although their orbital periods are shorter compared to more massive companions, they may experience extensive eclipses—up to 50% of the orbit—across all phases, particularly at lower frequencies (A. M. Archibald et al. 2009), although massive young companions have also been observed to be eclipsed, e.g., the PSR B1259-63 binary with an OB star (M. Chernyakova et al. 2021). This is due to intrabinary gas driven off the companion by pulsar wind irradiation, which can enshroud the pulsar in a highly gaseous environment. Consequently, such pulsars are only detected when the system is in a favorable orbital phase, specifically when the companion is near inferior conjunction. Although these eclipses and the associated DM variations hinder detections at lower frequencies (1–2 GHz), their behavior at higher frequencies, such as X band, remains less certain. If BLPSR resides in such an eclipsing binary system, its nondetection in subsequent observations may be due to orbital-phase-dependent occultation, with the initial detection having occurred during a more favorable orbital phase.

6.5.1. Intrinsic Emission Variability

Beyond external factors, several pulsars are known to exhibit pulsar nulling (V. Gajjar et al. 2012), an extreme form of emission suppression characterized by intermittent behavior where emission appears to intermittently switch off for several days (M. Kramer et al. 2006). Additionally, intermittency can significantly affect survey completeness; for example, if a pulsar is active for only 10% of the time and its nulling periods exceed the duration of a typical survey integration, there is only a 1% chance of detecting it both during the survey and in a follow-up confirmation observation (R. P. Eatough et al.

2013c). Although this intermittency phenomenon has been largely observed in canonical long-period isolated pulsars, it cannot be completely ruled out for MSPs. It is possible that BLPSR exhibits a similar intrinsic magnetospheric state-switching behavior, hindering its redetection in our later follow-up observations.

6.6. The "Missing Pulsar" Problem

Despite conducting one of the most sensitive and extensive pulsar surveys toward the GC to date, we did not conclusively detect any new pulsars, apart from the marginal BLPSR candidate, whose astrophysical origin remains uncertain. Under the assumption that the GC pulsar population resembles that observed in the rest of the Milky Way (J.-P. Macquart et al. 2010; J.-P. Macquart & N. Kanekar 2015), our survey—particularly the longer scans—should have been sensitive to a significant fraction of CPs (≈47%) and the brightest MSPs (≈9%) under weak-scattering conditions and when accounting for a typical beaming fraction of $f_b = 0.7$ (M. Kramer et al. 1998; see Section 6.2). Thus, the absence of such detections further deepens the longstanding "missing pulsar" problem in the GC (J. M. Cordes & T. J. W. Lazio 1997).

If BLPSR is not a pulsar, the implications are more severe: even the most luminous MSPs, expected to lie above our sensitivity thresholds, remain undetected. This suggests that the mechanisms potentially contributing to the marginal detection of BLPSR (see Section 6.5), such as highly eccentric orbits, variable scattering from a patchy screen, or intrinsic emission variability (e.g., nulling or intermittent emission states), may be widespread among the GC pulsar population. Although our searches probed a broad range of accelerations and orbital parameters, pulsars may still evade detection due to the unique challenges posed by the GC environment such as frequent dynamical interactions due to the high stellar density. As MSPs migrate inward via dynamical friction, close encounters with compact objects, including NSs and stellar- or intermediate-mass BHs, can disrupt pulsar binaries and eject them into unbound hyperbolic orbits (K. J. Li et al. 2022). Isolated pulsars can also be ejected. Additionally, NSs may be dynamically ejected from the central few parsecs due to either high natal kick velocities (O. Boodram & C. O. Heinke 2022) or gravitational interactions with massive stars within the central ∼1 pc (F. Abbate et al. 2018). Testing whether the innermost region of the GC is truly devoid of pulsars would require deeper surveys covering a broader area; however, detailed calculations of the likelihoods associated with these alternative nondetection scenarios are beyond the scope of the present work.

While the GC shares its extreme stellar density with globular clusters—where MSPs are abundant (R. Schödel et al. 2018)—its environment differs in key ways. It hosts an SMBH, has much higher velocity dispersion, and contains a younger and more massive stellar population. These factors likely lead to more frequent, violent dynamical interactions, increasing the likelihood of binary disruption and NS ejection rather than MSP retention and recycling. Additionally, as mentioned in Section 6.5, a pulsar's beam emission could precess away during its orbit, implying that caution must be used when it comes to dismissing possible pulsar candidates toward the GC, such as BLPSR (J.-P. Macquart et al. 2010). Thus, our null results (or marginal candidate) highlight both the observational challenges of detecting (and confirming) pulsars near Sgr A*, as well as the limitations of relying solely on deeper sensitivity.

Given that GC pulsars may only be briefly detectable during favorable scattering or orbital phases, we advocate for future surveys to prioritize regular, high-cadence monitoring over single ultradeep integrations. Capturing transient windows of visibility, such as those arising from refractive scintillation or specific orbital configurations that minimize eclipsing, may prove more effective than improving sensitivity alone. Sustained temporal coverage, rather than deeper integrations, may be the key to finally resolving the missing pulsar problem in the GC. If these efforts also fail, it may indicate that the weak-scattering case does not apply in the GC, or that the GC pulsar population near Sgr A* is very different from that of the Galactic field and globular clusters. This region might instead be dominated by magnetars, which are thought to account for 10%–50% of NS births in the Galaxy (E. F. Keane & M. Kramer 2008; J.-P. Macquart & N. Kanekar 2015).

7. Future and Ongoing Work

We conducted an additional 12 hr of follow-up observations on A00 with the GBT in 2024 January–February, using 2–3 hr scans to further investigate BLPSR; these data will be presented in a forthcoming publication. Ongoing analysis includes thorough acceleration and jerk searches, as well as the splitting of scans into 1 hr segments to account for a potential long orbital period (see Section 6.5). Future work will include computationally intensive coherent searches across subsequent scans and full epochs, as well as complementary single-pulse searches. In addition, we have recently observed 8.37 hr of Very Large Array (VLA) time in the D configuration at *X* band (synthesized beam of 7.″2 and $\Delta\nu = 4$ GHz). With a twofold sensitivity increase and 2 hr integration times, we expect a 6.5σ detection for BLPSR (rms noise of 3.48 μJy beam^{-1}) if this candidate is indeed a genuine pulsar and falls within the VLA synthesized beam. While these observations will initially focus on the innermost few arcseconds of the A00 region, future VLA proposals will aim to map the surrounding area. Additionally, the BL-GC survey with the GBT is continuing to collect data, with plans to expand to the *Ku*–*W* bands (12–93 GHz; see V. Gajjar et al. 2021). This comprehensive frequency coverage will be essential for detecting the most luminous pulsars near the GC. Such efforts will lay the groundwork for future pulsar detections with next-generation interferometers that will ultimately resolve the longstanding missing pulsar problem.

8. Conclusions

We have conducted one of the most sensitive pulsar surveys to date targeting the innermost (1.′4) region of the GC with the GBT at *X* band. Our observations, covering both short and long integrations of Sgr A* and its surrounding region (∼8′ diameter), reached sensitivities low enough to detect CPs and MSPs down to $L_{\rm min} \approx 0.14$ mJy kpc^2 and $L_{\rm min} \approx 0.26$ mJy kpc^2, respectively, assuming weak scattering. No pulsar candidates emerged in the short pointings, but we report a promising 8.19 ms MSP candidate, BLPSR, at a DM of 2775 pc cm^{-3} detected in the Epoch 1 long integrations during our $z_{\rm max} = 200$ acceleration searches.

BLPSR exhibited pulsarlike properties and was selected on its detection significance, high coherent power, and its temporal and

spectral characteristics after folding. We examined its characteristics by evaluating its S/N flux as a function of DM, and quantifying its signal persistence across both time and frequency using statistical KS tests. Randomizing the dataset and applying these KS tests yielded a false-alarm probability of $\sim 10^{-6}$, suggesting the candidate is unlikely to be a noise artifact. However, its low S/N, transient nature, and absence in subsequent scans and follow-up observations warrant caution. Further tests and observations are necessary to conclusively confirm or reject BLPSR as a pulsar.

The absence of a large pulsar population in our survey may point to observational biases—such as interstellar scattering, unfavorable pulsar beaming geometry, or binary-induced acceleration smearing—or suggest that pulsars near Sgr A* are intrinsically faint or exceptionally rare. Future surveys with greater sensitivity, longer integration times, and broader orbital phase coverage, such as those enabled by the midfrequency array of the Square Kilometre Array (SKA) Phase 1 and the full SKA (J.-P. Macquart & N. Kanekar 2015; R. Schoedel et al. 2024), will be critical to resolve any pulsars in the GC. Detecting, confirming, and timing a pulsar in a close orbit around Sgr A* remains a major goal for testing general relativity, understanding the SMBH, and probing the dense and turbulent environment at the heart of our Galaxy. Such surveys will ultimately reveal the long-hypothesized pulsar population or further deepen the missing pulsar problem in the GC.

Acknowledgments

We thank the anonymous referee for their review and for providing several suggestions and clarifications that improved the manuscript. We are also grateful to Prof. D. J. Helfand for a careful reading of the manuscript, and to Scott Ransom for his prompt and helpful responses on the PRESTO GitHub page. Breakthrough Listen is managed by the Breakthrough Initiatives, sponsored by the Breakthrough Prize Foundation. The Green Bank Observatory is a facility of the National Science Foundation operated under cooperative agreement by Associated Universities, Inc. We acknowledge use of computing resources from Columbia University's Shared Research Computing Facility project, which is supported by NIH Research Facility Improvement grant 1G20RR030893-01, and associated funds from the New York State Empire State Development, Division of Science Technology and Innovation (NYSTAR) Contract C090171, both awarded 2010 April 15.

Facility: GBT.

Software: PRESTO (S. M. Ransom 2001), dspsr (W. van Straten & M. Bailes 2011), PSRCHIVE (A. W. Hotan et al. 2004).

ORCID iDs

Karen I. Perez https://orcid.org/0000-0002-6341-4548
Vishal Gajjar https://orcid.org/0000-0002-8604-106X
Slavko Bogdanov https://orcid.org/0000-0002-9870-2742
Jules P. Halpern https://orcid.org/0000-0003-4814-2377
Paul B. Demorest https://orcid.org/0000-0002-6664-965X
Steve Croft https://orcid.org/0000-0003-4823-129X
Matt Lebofsky https://orcid.org/0000-0002-7042-7566
David H. E. MacMahon https://orcid.org/0000-0001-6950-5072
Andrew P. V. Siemion https://orcid.org/0000-0003-2828-7720

References

Abbate, F., Mastrobuono-Battisti, A., Colpi, M., et al. 2018, MNRAS, 473, 927
Abbate, F., Noutsos, A., Desvignes, G., et al. 2023, MNRAS, 524, 2966
Abuter, R., Amorim, A., et al. 2019, A&A, 625, L10
Ackermann, M., Ajello, M., Albert, A., et al. 2017, ApJ, 840, 43
Andersen, B. C., & Ransom, S. M. 2018, ApJL, 863, L13
Archibald, A. M., Stairs, I. H., Ransom, S. M., et al. 2009, Sci, 324, 1411
Bagchi, M., Lorimer, D. R., & Wolfe, S. 2013, MNRAS, 432, 1303
Barsdell, B. R., Bailes, M., Barnes, D. G., & Fluke, C. J. 2012, MNRAS, 422, 379
Boodram, O., & Heinke, C. O. 2022, MNRAS, 512, 4239
Brzycki, B., Siemion, A. P. V., de Pater, I., et al. 2024, AJ, 168, 284
Burgay, M., Bailes, M., Bates, S. D., et al. 2013, MNRAS, 433, 259
Cafardo, F., Nemmen, R. & Fermi LAT Collaboration 2021, ApJ, 918, 30
Chernyakova, M., Malyshev, D., van Soelen, B., et al. 2021, Univ, 7, 242
Clarke, N., Macquart, J.-P., & Trott, C. 2013, ApJS, 205, 4
Cordes, J. M., & Lazio, T. J. 1991, ApJ, 376, 123
Cordes, J. M., & Lazio, T. J. W. 1997, ApJ, 475, 557
Cordes, J. M., & Lazio, T. J. W. 2003, arXiv, arXiv:astro-ph/0301598
Cordes, J. M., & McLaughlin, M. A. 2003, ApJ, 596, 1142
Cromartie, H. T., Fonseca, E., Ransom, S. M., et al. 2020, NatAs, 4, 72
Della Monica, R., De Martino, I., & De Laurentis, M. 2023, MNRAS, 524, 3782
Deneva, J. S., Cordes, J. M., & Lazio, T. J. W. 2009, ApJ, 702, L177
Dexter, J., Deller, A., Bower, G. C., et al. 2017, MNRAS, 471, 3563
Dexter, J., & O'Leary, R. M. 2014, ApJL, 783, L7
Eatough, R., Karuppusamy, R., Kramer, M., et al. 2013a, ATel, 5040, 1
Eatough, R. P., Falcke, H., Karuppusamy, R., et al. 2013b, Natur, 501, 391
Eatough, R. P., Kramer, M., Lyne, A. G., & Keith, M. J. 2013c, MNRAS, 431, 292
Eatough, R. P., Torne, P., Desvignes, G., et al. 2021, MNRAS, 507, 5053
Faucher-Giguère, C.-A., & Loeb, A. 2011, MNRAS, 415, 3951
Figer, D. F., Rich, R. M., Kim, S. S., Morris, M., & Serabyn, E. 2004, ApJ, 601, 319
Fixsen, D. J. 2009, ApJ, 707, 916
Frayer, D. T. 2017, arXiv, arXiv:1704.00025
Gajjar, V., Joshi, B. C., & Kramer, M. 2012, MNRAS, 424, 1197
Gajjar, V., Perez, K. I., Siemion, A. P. V., et al. 2021, AJ, 162, 33
Gajjar, V., LeDuc, D., Chen, J., et al. 2022, ApJ, 932, 81
Genzel, R., Thatte, N., Krabbe, A., Kroker, H., & Tacconi-Garman, L. E. 1996, ApJ, 472, 153
Ghez, A. M., Salim, S., Hornstein, S. D., et al. 2005, ApJ, 620, 744
Heywood, I., Rammala, I., Camilo, F., et al. 2022, ApJ, 925, 165
Hotan, A. W., van Straten, W., & Manchester, R. N. 2004, PASA, 21, 302
Johannsen, T. 2016, CQGra, 33, 113001
Johnston, S., Kramer, M., Lorimer, D. R., et al. 2006, MNRAS, 373, L6
Keane, E. F., & Kramer, M. 2008, MNRAS, 391, 2009
Keith, M. J., Eatough, R. P., Lyne, A. G., et al. 2009, MNRAS, 395, 837
Knispel, B., Eatough, R. P., Kim, H., et al. 2013, ApJ, 774, 93
Kramer, M., Xilouris, K. M., Lorimer, D. R., et al. 1998, ApJ, 501, 270
Kramer, M., Lyne, A. G., O'Brien, J. T., Jordan, C. A., & Lorimer, D. R. 2006, Sci, 312, 549
Lazarus, P., Brazier, A., Hessels, J. W. T., et al. 2015, ApJ, 812, 81
Lazio, T. J. W., & Cordes, J. M. 1998, ApJ, 505, 715
Lebofsky, M., Croft, S., Siemion, A. P. V., et al. 2019, PASP, 131, 124505
Li, K. J., Wu, K., Leung, P. K., & Singh, D. 2022, MNRAS, 511, 3602
Liu, K., Wex, N., Kramer, M., Cordes, J. M., & Lazio, T. J. W. 2012, ApJ, 747, 1
Liu, K., Eatough, R. P., Wex, N., & Kramer, M. 2014, MNRAS, 445, 3115
Liu, K., Desvignes, G., Eatough, R. P., et al. 2021, ApJ, 914, 30
Lorimer, D. R., Bailes, M., Dewey, R. J., & Harrison, P. A. 1993, MNRAS, 263, 403
Lorimer, D. R., & Kramer, M. 2004, Handbook of Pulsar Astronomy, 4 (Cambridge Univ. Press)
Lower, M. E., Dai, S., Johnston, S., & Barr, E. D. 2024, ApJL, 967, L16
MacMahon, D. H. E., Price, D. C., Lebofsky, M., et al. 2018, PASP, 130, 044502
Macquart, J.-P., & Kanekar, N. 2015, ApJ, 805, 172
Macquart, J.-P., Kanekar, N., Frail, D., & Ransom, S. M. 2010, ApJ, 715, 939
Manchester, R. N., Lyne, A. G., D'Amico, N., et al. 1996, MNRAS, 279, 1235
Manchester, R. N., Hobbs, G. B., Teoh, A., & Hobbs, M. 2005, AJ, 129, 1993
Mezger, P. G., Zylka, R., Philipp, S., & Launhardt, R. 1999, A&A, 348, 457

Mori, K., Hailey, C. J., Schutt, T. Y. E., et al. 2021, ApJ, 921, 148
Muno, M. P., Pfahl, E., Baganoff, F. K., et al. 2005, ApJL, 622, L113
Nogueras-Lara, F., Schödel, R., Gallego-Calvente, A. T., et al. 2019, NatAs, 4, 377
O'Neil, K. 2002, in Single-Dish Radio Astronomy: Techniques and ApplicationsASPC278, 278, (ASP), 293
Pearlman, A. B., Majid, W. A., Prince, T. A., Kocz, J., & Horiuchi, S. 2018, ApJ, 866, 160
Perez, K. I., Bogdanov, S., Halpern, J. P., & Gajjar, V. 2023, ApJ, 952, 150
Pfahl, E., & Loeb, A. 2004, ApJ, 615, 253
Price, D. C., Flynn, C., & Deller, A. 2021, PASA, 38, e038
Psaltis, D., Wex, N., & Kramer, M. 2016, ApJ, 818, 121
Rajwade, K. M., Lorimer, D. R., & Anderson, L. D. 2017, MNRAS, 471, 730
Ransom, S. 2011, PRESTO: PulsaR Exploration and Search TOolkit, Astrophysics Source Code Library, ascl:1107.017
Ransom, S. M. 2001, PhD thesis, Harvard Univ.
Ransom, S. M., Eikenberry, S. S., & Middleditch, J. 2002, AJ, 124, 1788
Samsing, J., MacLeod, M., & Ramirez-Ruiz, E. 2017, ApJ, 846, 36
Schödel, R., Gallego-Cano, E., Dong, H., et al. 2018, A&A, 609, A27
Schoedel, R., Alberdi, A., Jimenez-Serra, I., et al. 2024, arXiv, arXiv:2406.04022
Scott, D. W. 1992, Multivariate Density Estimation: Theory, Practice, and Visualization (Wiley)
Spiewak, R., Bailes, M., Barr, E. D., et al. 2018, MNRAS, 475, 469
Sengar, R., Bailes, M., Balakrishnan, V., et al. 2024, MNRAS, 536, 3159
Spitler, L. G., Lee, K. J., Eatough, R. P., et al. 2014, ApJL, 780, L3
Stovall, K., Creighton, T., Price, R. H., & Jenet, F. A. 2012, ApJ, 744, 143
Suresh, A., Cordes, J. M., Chatterjee, S., et al. 2021, ApJ, 921, 101
Suresh, A., Cordes, J. M., Chatterjee, S., et al. 2022, ApJ, 933, 121
Torne, P., Desvignes, G., Eatough, R. P., et al. 2021, A&A, 650, A95
van Straten, W., & Bailes, M. 2011, PASA, 28, 1
Virtanen, P., Gommers, R., Oliphant, T. E., et al. 2020, NatMe, 17, 261
Wang, Q. D., Lu, F. J., & Gotthelf, E. V. 2006, MNRAS, 367, 937
Wang, Y., Creighton, T., Price, R. H., & Jenet, F. A. 2009a, ApJ, 705, 1252
Wang, Y., Jenet, F. A., Creighton, T., & Price, R. H. 2009b, ApJ, 697, 237
Wex, N., & Kopeikin, S. M. 1999, ApJ, 514, 388
Wharton, R. S., Chatterjee, S., Cordes, J. M., Deneva, J. S., & Lazio, T. J. W. 2012, ApJ, 753, 108
Yan, Z., Shen, Z.-Q., Wu, X.-J., et al. 2015, ApJ, 814, 5
Yao, J. M., Manchester, R. N., & Wang, N. 2017, ApJ, 835, 29
Zhao, J.-H., Morris, M. R., & Goss, W. M. 2020, ApJ, 905, 173